

Original Article

Cite this article: Sun Q-F, Wang K-Y, Sun F-Y, Zhang M, Zhao C-G, and Sun L-X (2022) Fluid evolution and ore genesis of Cu–Pb–Zn veins in the Panjiaduan deposit, Great Xing'an Range, NE China: evidence from fluid inclusion and H–O–He–Ar isotopes. *Geological Magazine* **159**: 1663–1680. <https://doi.org/10.1017/S0016756822000425>

Received: 4 October 2021

Revised: 16 April 2022

Accepted: 21 April 2022


First published online: 9 August 2022

Keywords:

Central Asian Orogenic Belt; Great Xing'an Range; Panjiaduan deposit; fluid inclusion; H–O–He–Ar isotopes

Author for correspondence: Ke-Yong Wang, Email: wangky@jlu.edu.cn

Fluid evolution and ore genesis of Cu–Pb–Zn veins in the Panjiaduan deposit, Great Xing'an Range, NE China: evidence from fluid inclusion and H–O–He–Ar isotopes

Qing-Fei Sun¹, Ke-Yong Wang^{1,2,3} , Feng-Yue Sun^{1,3}, Miao Zhang¹, Chen-Guang Zhao¹ and Li-Xue Sun¹

¹College of Earth Sciences, Jilin University, Changchun 130061, China; ²College of Geology and Mining Engineering, Xinjiang University, Urumqi 830047, China and ³MNR Key Laboratory of Mineral Resources Evaluation in Northeast Asia, Changchun 130061, China

Abstract

The southern Great Xing'an Range (SGXR), located in the eastern segment of the Central Asian Orogenic Belt (CAOB), is one of the most economically important Cu–Mo–Fe–Sn–Pb–Zn–Ag metallogenic provinces in China. The newly discovered Panjiaduan Cu–Pb–Zn deposit (9.3 Mt; at 1.36% Cu, 2.90% Pb, 3.80% Zn and 38.12 g/t Ag), located in the SE segment of the SGXR, is primarily hosted in fracture zones in volcanic rocks and granodiorite of the Manitu Formation. Four paragenetic stages of metallic mineralization are identified: (I) quartz-pyrite-arsenopyrite; (II) quartz-polymetallic sulphide; (III) quartz-galena-sphalerite-argentite; and (IV) quartz-calcite-minor sulphide. The hydrothermal quartz contains three types of primary fluid inclusion (FIs): vapour-rich two-phase liquid-vapour (LV-type), liquid-rich two-phase liquid-vapour (VL-type) and three-phase liquid-vapour-solid FIs (SL-type). Stages I and II contain all types with homogenization temperatures (T_h) of 324–386 °C and 276–334 °C as well as salinities of 0.7–38.0 wt% and 0.9–34.7 wt%, respectively, whereas stage III is composed of VL- and LV-type FIs with T_h of 210–269 °C and salinities of 0.5–7.2 wt%. Only VL-type FIs occur in stage IV, with T_h of 139–185 °C and salinities of 1.6–4.2 wt%. The $\delta^{18}\text{O}_{\text{H}_2\text{O}}$ and δD values vary from –15.7 to 2.6‰ and –132.7 to –110.2‰, respectively, indicating predominant meteoric water with an initial magmatic source. The He–Ar isotopic compositions of the pyrite inclusions from the Panjiaduan Cu–Pb–Zn veins suggest that fluids were derived from the crust.

1. Introduction

The southern Great Xing'an Range (SGXR), located in the eastern segment of the Central Asian Orogenic Belt (CAOB) (Fig. 1a, b), is one of the most economically important Cu–Mo–Fe–Sn–Pb–Zn–Ag metallogenic provinces in China (Chen & Li, 2009; Zeng *et al.* 2011; Ouyang *et al.* 2015). It comprises numerous porphyry Mo(–Cu), skarn Fe(–Sn), epithermal Au–Ag and hydrothermal vein-type Cu–Pb–Zn–Ag ore deposits (e.g. Wang *et al.* 2001; Zeng *et al.* 2011, 2015; Ouyang *et al.* 2014, 2015; Shu *et al.* 2016; Chen *et al.* 2017; Zhai *et al.* 2018a, b; Ma *et al.* 2019). The region can be divided into the Xilinhaote–Xilinguole Ag–Pb–Zn, Huanggangliang–Ganzhuermiao Fe–Sn–Cu–Pb–Zn and Tianshan–Tuquan Cu polymetallic sub-metallogenic belts (from NW to SE) (Fig. 1c; Liu *et al.* 2004). Earlier studies primarily focused on the mineralogy and geochronology as well as the nature, origin and evolution of the ore-forming fluids of ore deposits in the first two metallogenic belts (e.g. the Hashitu Mo porphyry, Baiyinnuoer Pb–Zn skarn, Huanggang Sn–Fe skarn, Haobugao Fe–Zn skarn, Weilasituo Zn–Cu–Ag vein, Bairendaba Ag–Zn–Pb vein and Bianjiadayuan Ag–Pb–Zn vein deposits; Zhou *et al.* 2012; Ouyang *et al.* 2014; Mei *et al.* 2015; Shu *et al.* 2013, 2016, 2020; Liu *et al.* 2016b, 2017; Zhai *et al.* 2017, 2018b; Gao *et al.* 2019). Previously published studies have indicated that the majority of these deposits are genetically related to spatially associated Mesozoic granites. However, the genesis of the deposits in the Tianshan–Tuquan Cu polymetallic metallogenic belts, especially for the base metal veins, are as yet unknown or still under debate (Gu, 2016; Shi *et al.* 2020; Yang *et al.* 2020; Sun *et al.* 2021).

The SGXR contains several recently discovered vein-type deposits, including the Bianjiadayuan Ag–Pb–Zn, Weilasituo Zn–Cu–Ag, Bairendaba Ag–Zn–Pb, Shuangjianzishan Ag–Pb–Zn, Dajing Cu–Sn and Meng'entaolegai Ag–Pb–Zn deposits (Fig. 1c; Wang *et al.* 2006; Ouyang *et al.* 2014; Liu *et al.* 2016a, b; Zhai *et al.* 2017; Yang *et al.* 2020). Previous studies of the base metal veins in the Xilinhaote–Xilinguole and Huanggangliang–Ganzhuermiao zones suggested that fluid mixing, dilution and cooling are the most important factors for ore deposition (e.g. Ouyang *et al.* 2014; Li *et al.* 2017; Zhai *et al.* 2018b). However, whether the base metal

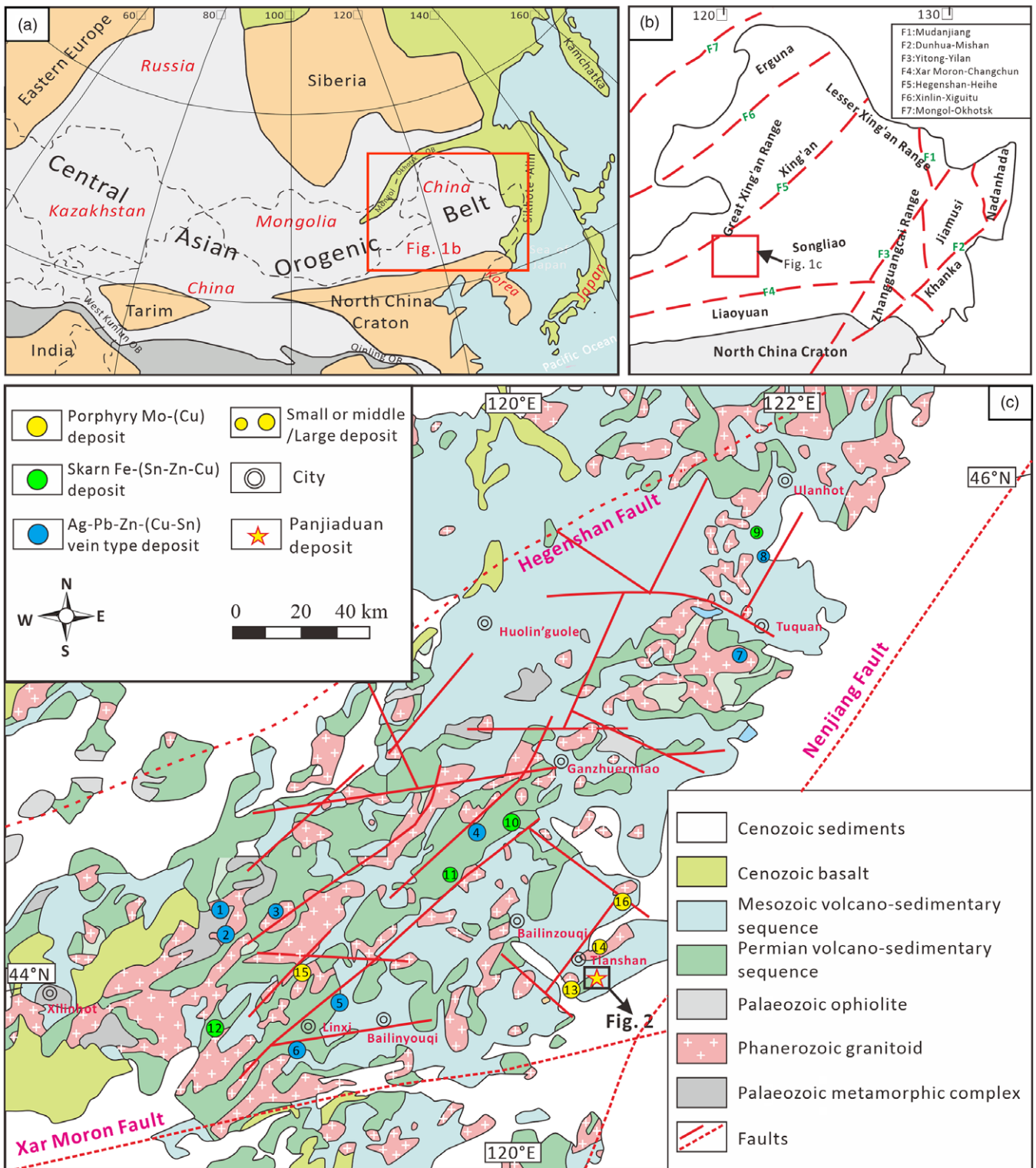


Fig. 1. (Colour online) (a) Simplified tectonic map showing the location of NE China, modified after Safonova & Santosh (2014). (b) Tectonic map of NE China (after Wu *et al.* 2011a, b); and (c) geologic map of the southern Great Xing'an Range (after Ouyang *et al.* 2014). Deposit symbols: 1, Weilasituo Zn–Cu–Ag; 2, Bairendaba Ag–Pb–Zn; 3, Shabulengshan Cu–Zn; 4, Shuangjianzishan Ag–Pb–Zn; 5, Dajing Cu–Sn; 6, Bianjiadayuan Ag–Pb–Zn; 7, Meng'entaolegai Ag–Pb–Zn; 8, Lianhuashan Cu; 9, Shenshan Fe–Cu; 10, Haobugao Fe–Zn; 11, Baiyinnuoer Pb–Zn; 12, Huanggang Fe–Sn; 13, Laojiagou Mo; 14, Banlashan Mo; 15, Hashitu Mo; 16, Aolunhua Mo–Cu.

veins in the Tianshan–Tuquan Cu polymetallic metallogenic belts also formed according to the above processes is unknown. To address this, we conducted a detailed study on the geology, mineralogy, fluid inclusion (FI) and isotopes (H, O, He and Ar) of

the newly discovered Panjiaduan deposit, which is located in the Tianshan area (Fig. 1c). This deposit contains ore reserves of over 9.3 Mt, grading 1.36% Cu, 2.90% Pb, 3.80% Zn and 38.12 g/t Ag. To further guide mineral exploration of the base metal vein-type

deposits in the SGXR, we compared isotope data from the present study with those from Pb–Zn–(Cu–Ag) vein deposits (associated with granitoids) elsewhere in the world.

2. Geological setting

The SGXR is located in the southeastern region of Inner Mongolia and bordered by the Erlian-Hegenshan fault in the north, the Xar Moron fault in the south and the Nenjiang fault in the east (Fig. 1b). The region has undergone multiphase Phanerozoic tectonic events, including (1) the Palaeozoic – early Mesozoic subduction and final closure of the Palaeo-Asian Ocean (Robinson *et al.* 1999; Xiao *et al.* 2003; Wu *et al.* 2011a); (2) the Mesozoic S-dipping subduction and final closure of the Mongol-Okhotsk Ocean (Sorokin *et al.* 2004; Donskaya *et al.* 2013); and (3) the Mesozoic W-dipping region of the Palaeo-Pacific subduction zone (Xu *et al.* 2013; Wilde, 2015). The exposed strata in the area comprise an early Palaeozoic metamorphic complex and ophiolite, late Palaeozoic and Mesozoic volcano-sedimentary sequences, and Cenozoic sediments (Fig. 1c). The Palaeozoic Xilinhote complex comprising plagioclase-biotite gneiss, granitic gneiss, schist and minor amphibolite hosts the Weilasituo and Bairendaba Pb–Zn–(Cu–Ag) veins (Liu *et al.* 2016b). The upper Palaeozoic volcano-sedimentary sequence is primarily composed of the Permian Shoushangou, Dashizhai, Zhesi and Linxi formations, and hosts numerous base metal veins and skarn deposits (e.g. the Shenshan Fe–Cu, Dajing Cu–Sn, Haobugao Fe–Zn and Bianjiadayuan Ag–Pb–Zn deposits; Wang *et al.* 2006; Ouyang *et al.* 2014; Zhai *et al.* 2017; Ma *et al.* 2019; Shu *et al.* 2020). The widely distributed Mesozoic volcano-sedimentary rocks are controlled by regional NE-trending faults. These rocks include the Lower Jurassic Hongqi formation, Middle Jurassic Wanbao and Xinmin formations, Upper Jurassic Manketouebo, Manitu and Baiyin'gaolao formations, and the minor Lower Cretaceous Meiletu formation. The Cu–Pb–Zn–Mo mineralization in the Tianshan-Tuquan zone is primarily hosted in the Middle–Upper Jurassic sequences (e.g. the Banlashan Mo, Shabulengshan Cu–Zn and Lianhuashan Cu deposits; Zhang *et al.* 2010; Gu, 2016; Zhang, 2017).

Phanerozoic magmatism occurred in five stages: (1) late Carboniferous (c. 320–305 Ma), (2) early Permian (c. 285–270 Ma), (3) Middle–Late Triassic (c. 247–218 Ma), (4) Early–Middle Jurassic (c. 182–175 Ma) and (5) Late Jurassic – Early Cretaceous (c. 161–125 Ma) (Gu, 2016; Zhang, 2017; Ma *et al.* 2019). The Middle–Late Triassic intrusive rocks, which comprise tonalite, granodiorite and monzogranite, are spatially and temporally related to porphyry-skarn-epithermal Cu–Mo–Pb–Zn mineralization (e.g. the Baiyinnuoer Pb–Zn skarn, Laojiagou Mo porphyry and Lianhuashan high-sulphidation epithermal Cu deposits; Shu *et al.* 2013; Gu, 2016; Tang *et al.* 2019). The Late Jurassic – Early Cretaceous intrusive rocks, including granodiorite, plagioclase granite and syenogranite, are widespread in the region and genetically related to the late Mesozoic polymetallic mineralization (c. 133–165 Ma; Zhou *et al.* 2012; Zhai *et al.* 2017; Liu *et al.* 2016a, b; Ma *et al.* 2019; Shu *et al.* 2020; Shi *et al.* 2020).

3. Ore deposit geology

3.a. Stratigraphy and structures

The strata exposed near the Panjiaduan deposit primarily includes the Upper Jurassic Manitu Formation and Quaternary sediments

(Fig. 2a). The Manitu Formation comprises andesite, intermediate-felsic tuff and tuffaceous sandstone dipping to the east at 30–40°, with a U–Pb zircon age of c. 138–158 Ma (Sun *et al.* 2011; Zhang *et al.* 2017). The Cu–Pb–Zn veins associated with the deposit are predominantly hosted by the intermediate-felsic tuff of the Manitu Formation (Fig. 2a). These volcanic rocks have a calc-alkaline affinity, and are large-ion lithophile element (LILE-) enriched, high-field-strength element (HFSE-) depleted and possess a relatively low initial $^{87}\text{Sr}/^{86}\text{Sr}$ ratio ($(^{87}\text{Sr}/^{86}\text{Sr})_i = 0.70441\text{--}0.70492$), positive $\epsilon_{\text{Nd}}(t)$ (0.16–1.64) and young T_{DM2} model ages (694–767 Ma) (Zhang *et al.* 2017). The E–W-trending faults and secondary NW- and NE-trending faults are the primary structures in the ore district. They principally developed in the central and eastern parts of the district within the Manitu Formation. Among these faults, the EW-trending faults (> 800 m long, c. 10 m wide and S-dipping (70–80°)) host hydrothermal breccias in the Manitu Formation. The NW-trending faults (> 400 m long and 1–5 m wide) are the vein-type Cu–Pb–Zn ore-controlling structures. These faults are steeply SW-dipping (70–85°), while the NE-trending faults are smaller (50–100 m long and 1–2 m wide) and NW-dipping (55–70°).

The dominant igneous rocks spatially associated with the Panjiaduan deposit consist of granodiorite and syenogranite, as well as diorite and granite porphyry dykes (Fig. 2a). The granodiorite batholith is found in the southern region of the Panjiaduan deposit and comprises quartz (25–30%), plagioclase (45–50%), K-feldspar (10–15%) and minor (5–10%) altered biotite (Sun *et al.* 2021). The syenogranite batholith is exposed in the western region of the Panjiaduan deposit and consists of quartz (c. 25%), plagioclase (c. 15%), K-feldspar (40–45%) and altered biotite (10–15%), and hosts several Late Triassic porphyry-type Mo deposits (Sun *et al.* 2021). There are also minor NNE- and NE-trending diorite and granite porphyry dykes (> 150 m long and 1–4 m wide) that intruded volcanic rocks of the Manitu Formation (Fig. 2a).

3.b. Mineralization and alteration

The Cu–Pb–Zn veins in the Panjiaduan deposit occur in fracture zones in the Manitu Formation and granodiorite (Fig. 2a–c). Numerous vein/veinlet and breccia ores have been identified in the ore district. Eight NE-, NW- and EW-trending Cu–Pb–Zn orebodies are found in the SE region of the Panjiaduan deposit. The NE-trending Pb–Zn orebodies (Nos 2 and 5) strike 60–64° and dip at 58–65° SW. These orebodies are 100–560 m long, 4–5 m thick, and together contain 0.86% Cu, 1.78% Pb and 1.81% Zn. The NW-trending Cu–Pb–Zn orebodies (Nos 1, 1-1, 1-2 and 3) occur as NW-trending open-space veins in the granodiorite that are steeply NE-dipping (75–80°). These orebodies are 243–500 m long (average thicknesses of 1–9 m) with an average grade of 1.7% Cu, 3.56% Pb and 4.64% Zn. The roughly EW-trending Cu–Pb–Zn orebodies (Nos 4 and 9) are moderately N-dipping (58–70°). They are 100–500 m long, 4–6 m thick, 278–633 m deep, and have an average grade of 2.21% Cu, 4.45% Pb and 5.72% Zn.

The metallic minerals included in the deposit include pyrite, chalcopyrite, sphalerite, galena and haematite, with minor arsenopyrite, argentite and bornite (Fig. 3). The non-metallic minerals comprise quartz, chalcedony, hornblende, sericite, chlorite, epidote and calcite. The alteration zone is up to 10 m wide and consists primarily of silicic, propylitic (epidote-chlorite), sericitic, carbonate and (minor) pyritization that is spatially confined to the NW/E–W-trending faults (Fig. 3a–i). Among them, silicification is the

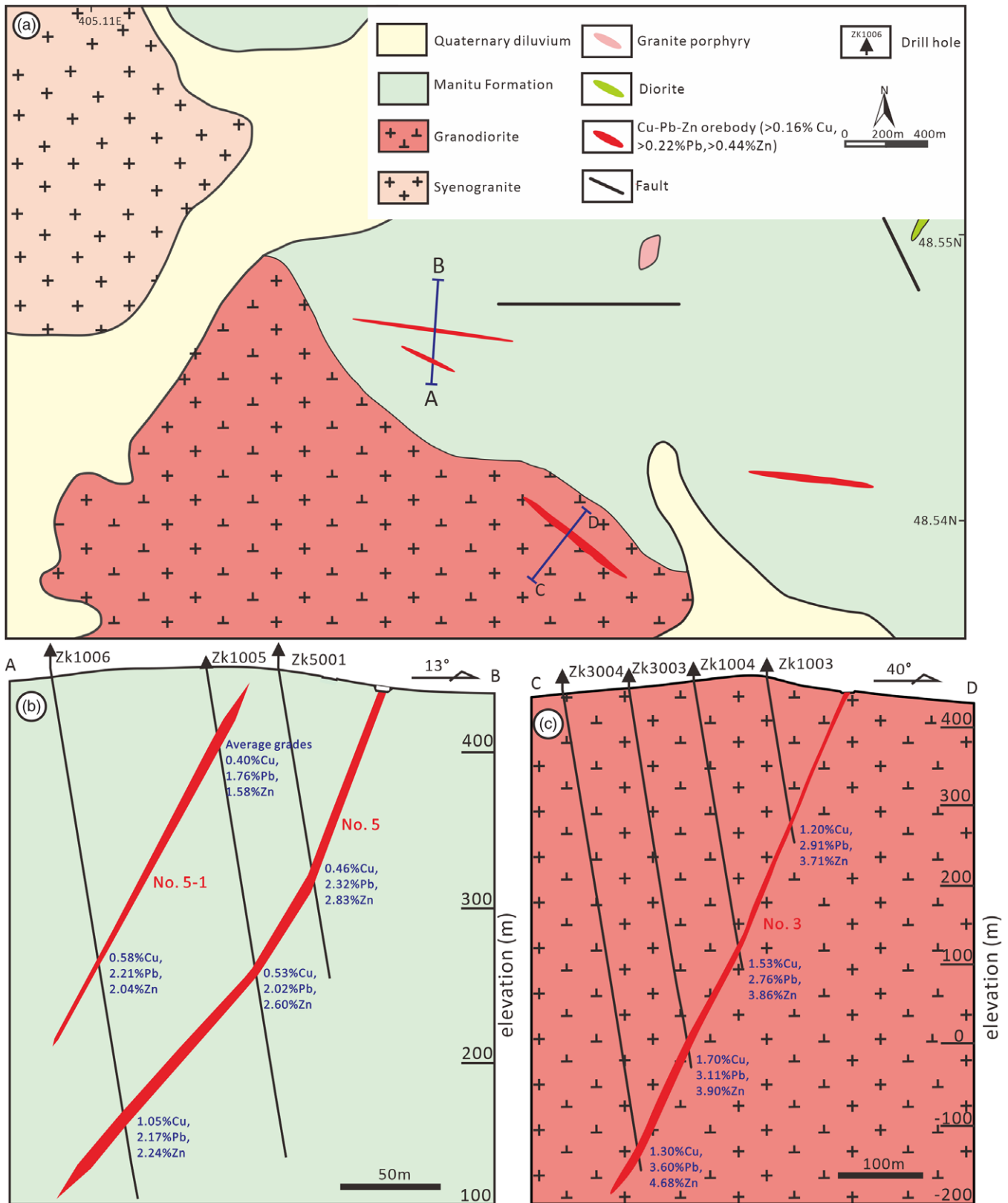


Fig. 2. (Colour online) (a) Geologic map of the Panjiaduan deposit. Cross-section of the vein-type Cu-Pb-Zn orebodies in (b) volcanic rocks of Manitu Formation and (c) granodiorite.

most pervasive and Cu-Pb-Zn ore-related alteration style, and it strongly occurs in the granitoid as well as the rocks in the Manitu Formation. In addition, it commonly coexists with carbonate,

sericitic and pyrite types of alteration within the granodiorite. Chloritization and epidotization strongly occur in the volcanic rocks and, to a lesser extent, intrusive rocks in the Manitu

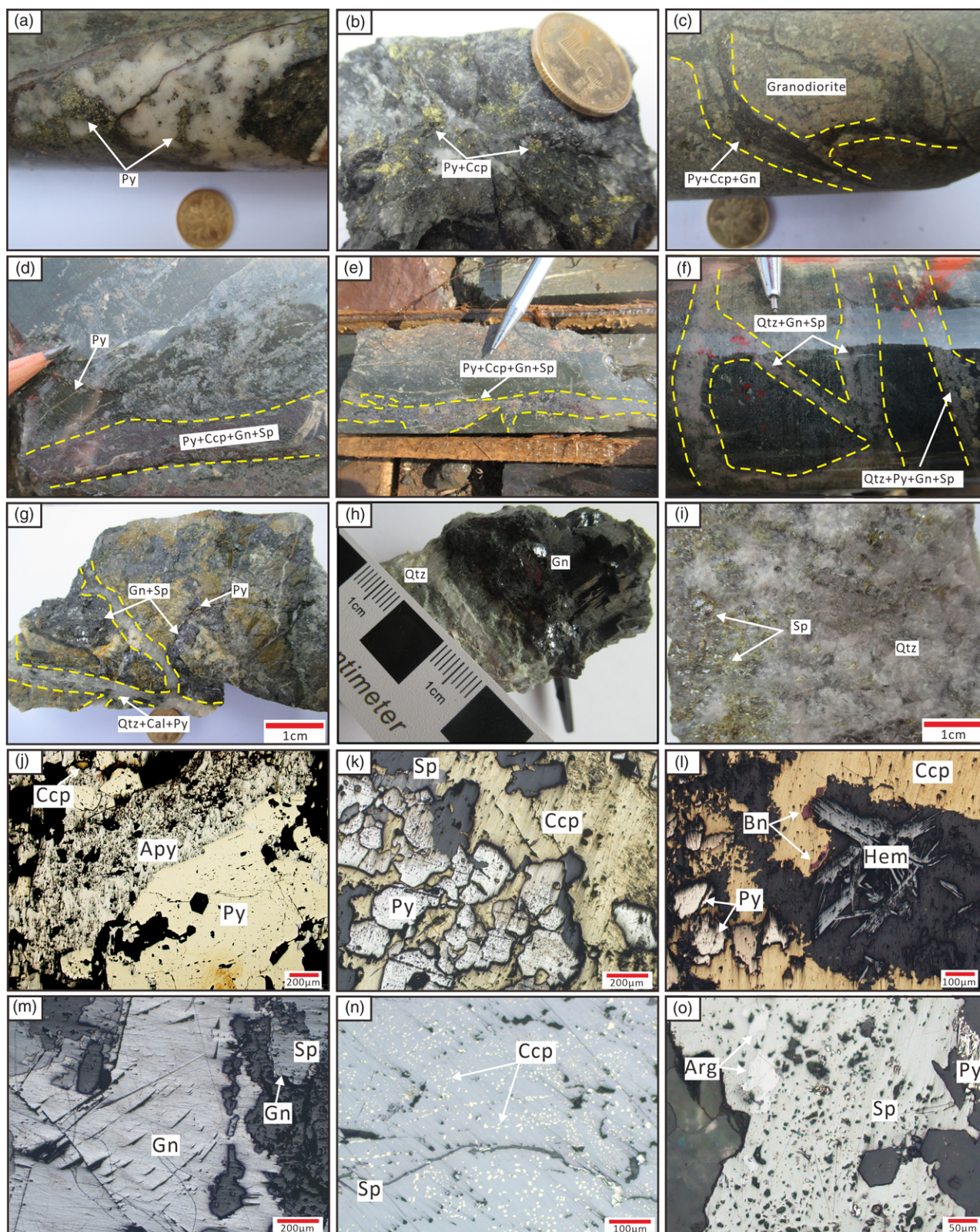


Fig. 3. (Colour online) Photographs of the Panjiaduan Cu-Pb-Zn deposit: (a) stage I quartz-pyrite-(arsenopyrite) vein; (b) stage II quartz-pyrite-chalcopyrite ore; (c) stage II polymetallic sulphides hosted in granodiorite; (d, e) stage II polymetallic sulphides hosted in volcanic rocks of Manitu Formation; (f) stage III quartz-pyrite-galena-sphalerite veins; (g) stage III brecciated galena-sphalerite ores; (h) stage II coarse-grained euhedral galena; (i) stage III greenish fine-grained anhydrous sphalerite in milky quartz veins; (j) stage I subhedral pyrite-arsenopyrite with minor chalcopyrite; (k) stage II anhydrous chalcopyrite and sphalerite replaced subhedral pyrite; (l) supergene haematite and bornite replaced stage II anhydrous chalcopyrite; (m) stage III subhedral galena replaced anhydrous sphalerite; (n) stage III chalcopyrite disease occurs in sphalerite; and (o) stage III sphalerite and argentite assemblages replaced pyrite. Apy – arsenopyrite; Arg – argentite; Bn – bornite; Cal – calcite; Ccp – chalcopyrite; Gn – galena; Hem – haematite; Py – pyrite; Qtz – quartz; Sp – sphalerite.

Formation, and are associated with silver-bearing metal sulphide mineralization.

3.c. Paragenetic sequence

Based on field investigations as well as mineral assemblages and cross-cutting relationships, four paragenetic stages of Cu–Pb–Zn mineralization are recognized here (Fig. 4). Late supergene oxidation affected the primary sulphides to form haematite, bornite, covellite and malachite (Fig. 3l).

Stage I is the earliest stage and is characterized by quartz, pyrite and minor arsenopyrite. Pyrite occurs as coarse-grained euhedral sizes within altered volcanic rocks and subhedral aggregates in milky quartz veins, whereas arsenopyrite generally occurs as fine-grained anhedral aggregates with pyrite in milky quartz veins (Fig. 3a, j). Both are commonly replaced by aggregates of chalcopyrite and sphalerite during stage II (Fig. 3b).

Stage II (quartz-polymetallic sulphide) is characterized by the presence of large amounts of sulphides (pyrite, chalcopyrite, galena, sphalerite and minor bornite) within fractures in altered volcanic rocks and white-grey quartz veins (Fig. 3b–e). Chalcopyrite principally occurs as anhedral aggregates with pyrite and fills microcracks within the pyrite. Bornite is included in chalcopyrite that coexist with haematite (Fig. 4l), indicating a supergene process. Galena characteristically occurs as coarse-grained euhedral cubes, while sphalerite generally occurs as coarse-grained brown subhedral aggregates (Fig. 3h).

Stage III (quartz-galena-sphalerite-argentite) is composed primarily of quartz, galena and sphalerite, with minor calcite, pyrite, chalcopyrite and argentite that commonly occur in breccias and veins (Fig. 3f, g). Sphalerite occurs as fine-grained greenish anhedral aggregates in white-grey quartz veins (Fig. 3l), while galena occurs as fine-grained anhedral aggregates (Fig. 3m; Sun *et al.* 2021). Minor chalcopyrite disease occurs in the sphalerite (Fig. 4n). Argentite is the only Ag-bearing mineral observed in the deposit, where it occurs as inclusions within the sphalerite (Fig. 4o).

Stage IV (quartz-calcite-minor sulphide) is represented by quartz, calcite and minor amounts of pyrite and sphalerite within fractured zones in altered volcanic rocks (Sun *et al.* 2021). Quartz-calcite veins commonly contain earlier galena-sphalerite breccia. These veins generally indicate that quartz crystals grew from the walls towards the centre, with later infilling of calcite crystals and minor pyrite (Sun *et al.* 2021). This observation implies that the formation of quartz occurred slightly earlier than that of calcite, although they likely precipitated from the same fluid system.

4. Sampling and analytical methods

4.a. Fluid inclusion analyses

To help constrain the conditions of ore formation of the Cu–Pb–Zn veins, quartz from each sulphide-bearing stage was made into doubly polished thin-sections (< 0.30 mm thick) for FI petrographic, microthermometric and laser Raman spectroscopic analyses. Microthermometric and laser Raman spectroscopic analyses were conducted at the Key Laboratory of Geological Fluids, Jilin University, Changchun, China using a Linkam THMS-600 heating–freezing stage (–196 to 600 °C), a Renishaw RM1000 Raman microprobe and an Ar ion laser. The microthermometric equipment was calibrated by the freezing point of pure water (0.0 °C) (Sternner & Bodnar, 1984). The precision of each microthermometric measurement was ± 0.2 °C during cooling cycles and ± 0.1 °C during heating cycles. The temperatures of these cycles and phase transitions were

determined at heating rates of 1–5 °C/min and 0.1–0.5 °C/min, respectively. The Raman shift was calibrated using a single silicon crystal. The operating conditions for the Raman microprobe included a laser power of 5 mW, a laser wavelength of 514.5 nm, a beam diameter of 1–2 μm and a counting time of 30 s. The procedure for the laser Raman spectroscopic measurement was given by Wopenka *et al.* (1990).

4.b. Isotope analysis

4.b.1. H–O isotopes

Hydrogen and oxygen isotopic analyses of the FIs in quartz from the four metallic mineral stages were conducted at the Beijing GeoAnalysis Co. Ltd, China using a Finnigan MAT-253 mass spectrometer (Clayton & Mayeda, 1963). The samples used for hydrogen and oxygen isotope analyses contained approximately 60–85% primary FIs and between 15 and 40% secondary inclusions, the former of which increased from stage I to stage IV. Before hydrogen isotope analysis, the samples were crushed to a granularity of 40–60 mesh and then heated to 100–200 °C to decrepitate a majority of the secondary FIs and thereby largely eliminate their contribution to the isotope composition. The dried samples were then put into a Flash EA, Thermo at 1420 °C to decrepitate the FIs. The hydrogen for isotopic analysis was then loaded into the mass spectrometry by high pure helium. The samples for oxygen isotope analysis were crushed to a granularity of 200 mesh and then put into the oven at 105 °C for 12 hours. Oxygen was extracted from the quartz through BrF_5 reactions in a vacuum under high temperature (580 °C) conditions and then collected using a 5 Å molecular sieve sample tube. The isotopic ratios for oxygen and hydrogen are presented in standard δ notation (‰) relative to Standard Mean Ocean Water (SMOW) with an analytical precision of $\pm 0.2\text{‰}$ in $\delta^{18}\text{O}$ and $\pm 2\text{‰}$ in δD , respectively.

4.b.2. He–Ar isotopes

Four pyrite samples from stages II and III were analysed for He and Ar isotopic compositions. The analyses were performed using a Nobleless SFT mass spectrometer at the Key Laboratory of Petroleum Resources, Northwest Institute of Eco-Environment and Resources, CAS, Lanzhou, China. Noble gases were selected by heating in a vacuum; we then also used liquid nitrogen, a sponge titanium furnace (800 °C) and a Zr–Al getter pump to further separate the noble gases. The purified noble gases were separated into He–Ne and Ar gases using a cold pump. The noble gas isotope composition of the reference samples included a ^4He content of 5.24×10^{-6} (V/V), ^{20}Ne content of 1.68×10^{-5} (V/V), ^{40}Ar content of 9.31×10^{-3} (V/V), $^3\text{He}/^4\text{He}$ ratio of 1×10^{-6} , $^{40}\text{Ar}/^{36}\text{Ar}$ ratio of 295.5 and $^{38}\text{Ar}/^{36}\text{Ar}$ ratio of 0.188.

5. Results

5.a. Fluid-inclusion petrography

During the detailed petrographic observations a large number of FIs, including primary, pseudosecondary and secondary FIs, were found in quartz from stages I to IV. According to the criteria of Roedder (1984), a pseudosecondary assignment was recognized as those present in the planes of inclusions terminated within a crystal, whereas secondary inclusions were assigned to those planes that cross-cut grain boundaries (Fig. 5j, k). Pseudosecondary and secondary inclusions consist of two-phase liquid–vapour inclusions. The secondary inclusions are generally < 10 μm in diameter with low vapour percentage of

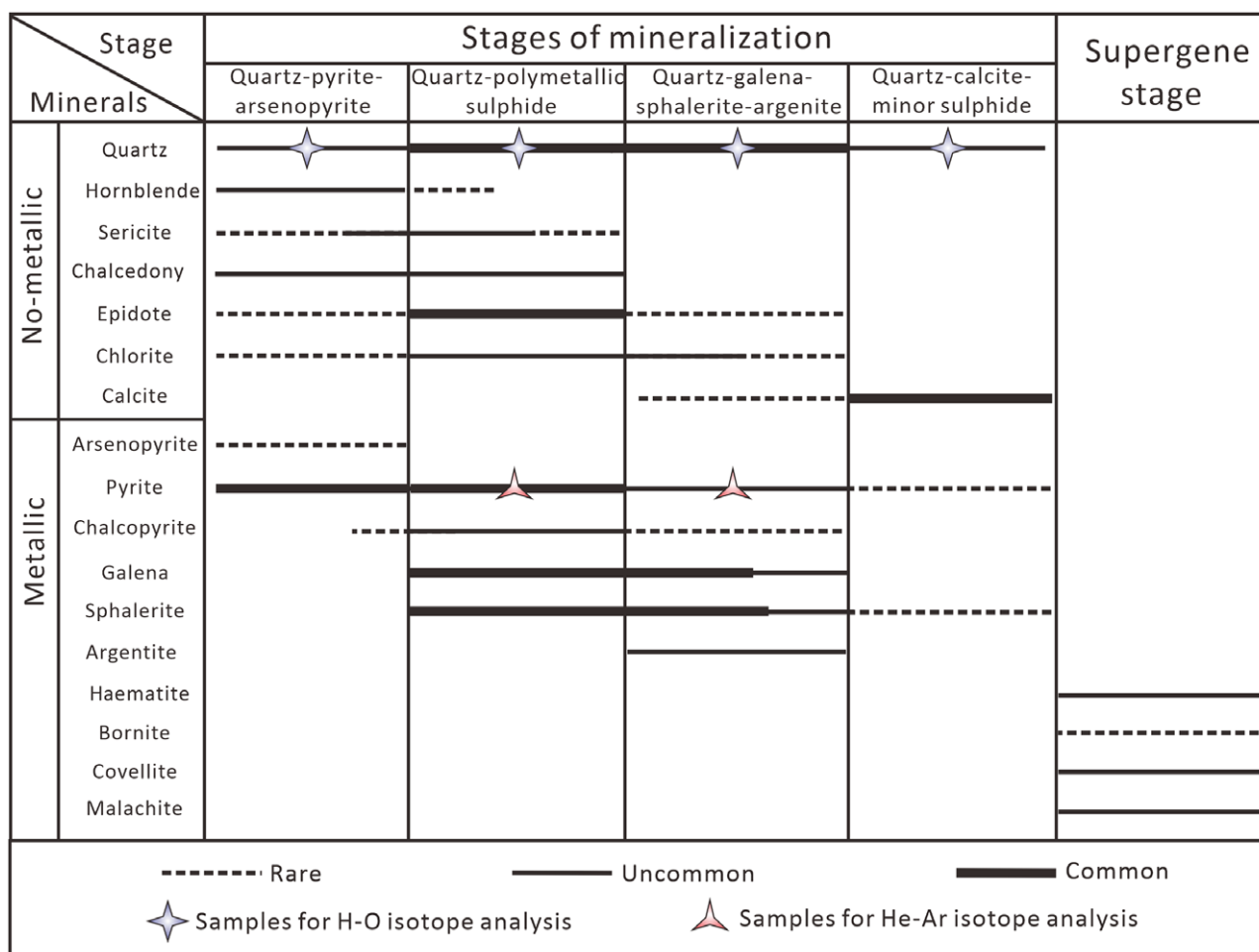


Fig. 4. Summary of paragenetic stages for the Panjiaduan Cu-Pb-Zn mineralization.

5–10 vol.%. The primary FIs can be classified into three types (Fig. 5), based on their vapour-to-liquid ratios at room temperature (25 °C), heating-freezing behaviour and the compositions determined by laser Raman spectroscopy.

Liquid-rich two-phase liquid-vapour FIs (VL-type) are the most abundant type of primary inclusions in the various mineralized stages (Fig. 5c-l). They typically have two phases at room temperature and are predominantly liquid-rich with the vapour percentage of 10–30 vol.%. These FIs vary from < 10 to 30 µm in diameter with elongated, elliptical or irregular shapes. FIs of this type are principally abundant in stages I–IV quartz and are either clustered or isolated. They also coexist with vapour-rich two-phase liquid-vapour FIs (LV-type) and three-phase liquid-vapour-solid FIs (SL-type) as boiling FI assemblages in stages I–III.

LV-type FIs are two-phase inclusions at room temperature with a high vapour percentage of 70–85 vol.% (Fig. 6b-i). They are approximately 10–25 µm in diameter and are typically spherical or elliptical in shape. LV-type FIs are primarily clustered in quartz in stages I–III, where they coexist with VL-type and SL-type FIs.

SL-type FIs contain liquid and vapour as well as opaque and transparent daughter minerals at room temperature (Fig. 6c, f, g). The transparent daughter mineral occurs as subhedral/euhedral cubes and is likely halite. These inclusions are generally 5–20 µm in diameter with negative crystal, elliptical and irregular shapes. They contain 5–10 vol.% daughter minerals with the

vapour percentage 5–25 vol.%, and occur clustered and isolated in quartz in stages I and II.

5.b. Microthermometry and laser Raman spectroscopy

Microthermometric studies were conducted on various types of primary, pseudosecondary and secondary inclusions in the quartz in stages I–IV. The secondary inclusions generally homogenize into the liquid phase at 108–175 °C (stage I), 109–164 °C (stage II), 109–148 °C (stage III) and 103–129 °C (stage IV). As the phase transition of LV-type FIs was difficult to observe, the ice-melting temperatures (T_{m-ice}) are not particularly precise. The microthermometric data calculated by the MacFlinCor calculation program (Brown & Hagemann, 1995) are summarized in Table 1 and illustrated in Figure 6.

Stage I: The VL-type FIs characteristically homogenize into the liquid phase with vapour disappearance temperatures of 324–380 °C. They have T_{m-ice} between –12.1 and –7.0 °C with corresponding salinities of 10.5–16.1 wt% NaCl equiv. The LV-type FIs have T_h of 337–365 °C (liquid phase disappearance), T_{m-ice} of –1.9 to –0.4 °C, and corresponding low salinities of 0.7–3.2 wt% NaCl equiv. The SL-type FIs homogenize to the liquid phase at 348–386 °C with halite dissolution temperatures of 251–298 °C and salinities of 34.7–38.0 wt% NaCl equiv.

Stage II: The VL-type FIs have T_h of 278–330 °C and T_{m-ice} of –8.9 to –5.0 °C with salinities of 7.9–12.8 wt% NaCl equiv. The

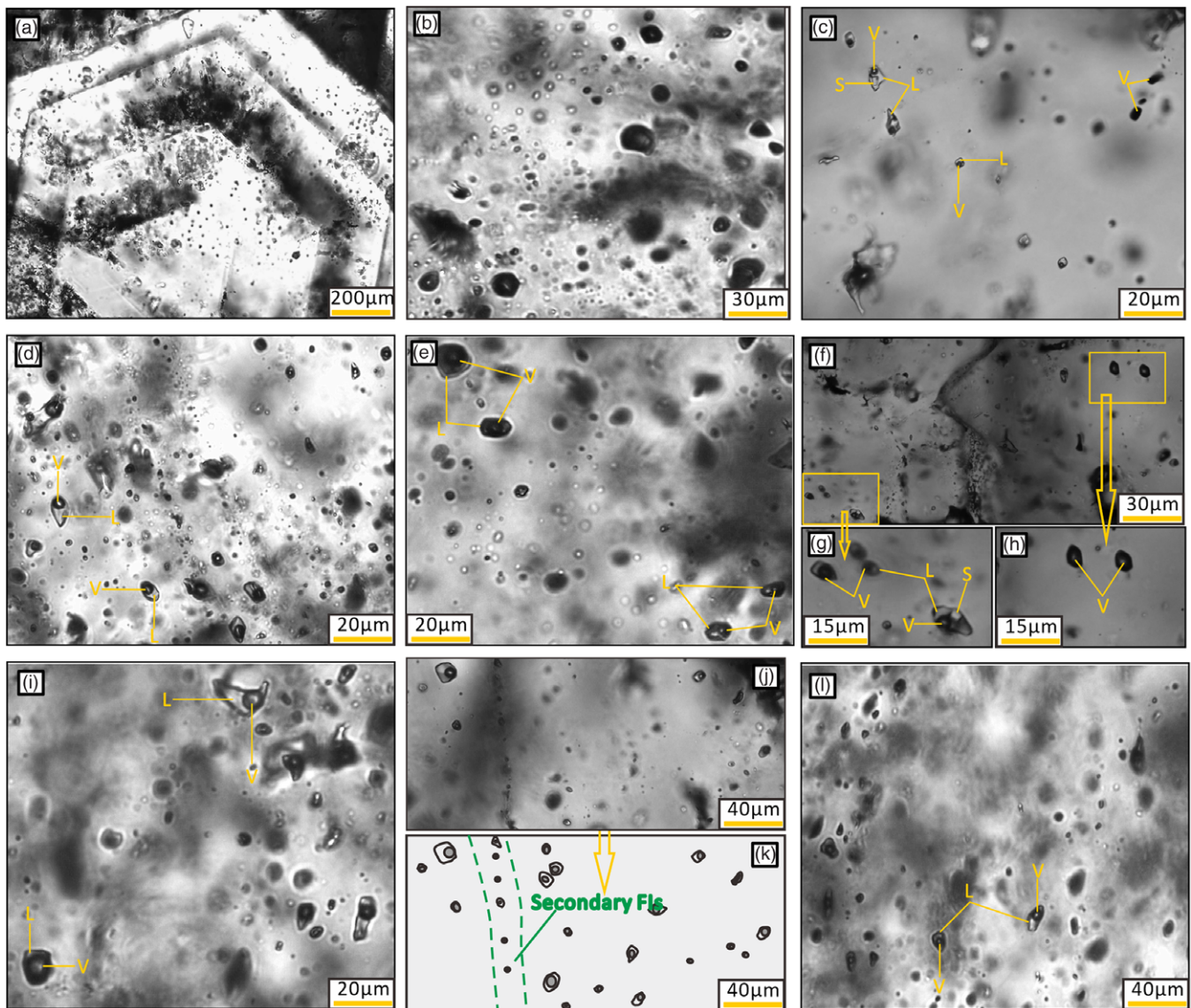


Fig. 5. (Colour online) Photomicrographs showing the types and distribution of FIs from the Panjiaduan deposit: (a) obvious euhedral growth zones observed in stage I hydrothermal vein quartz associated with sulphide deposition; (b) LV-type FIs in stage I quartz; (c) LV- and SL-type FIs coexisting in stage I quartz; (d) VL-type FIs in stage II quartz; (e) VL- and LV-type FIs coexisting in stage II quartz; (f–h) VL-, LV- and SL-type FIs coexisting in stage II quartz; (i–k) VL- and LV-type FIs coexisting in stage III quartz; and (l) VL-type FIs in stage IV quartz. L – liquid; V – vapour; S – halite daughter mineral.

LV-type FIs homogenize to the gaseous phase between 276 and 319 °C with T_{m-ice} of -1.8 to -0.5 °C and salinities of 0.9–3.1 wt% NaCl equiv. The SL-type FIs have halite dissolution temperatures of 210–250 °C with corresponding salinities of 32.4–34.7 wt% NaCl equiv. They homogenize to the liquid phase at temperatures of 283–334 °C.

Stage III: Only VL- and LV-type FIs were identified in the mineralized quartz crystals. The VL-type FIs have T_h of 216–265 °C and T_{m-ice} of -4.5 to -2 °C with salinities of 3.4–7.2 wt% NaCl equivalent. The LV-type FIs homogenize into the vapour phase of 210–269 °C with T_{m-ice} of -1.6 to -0.3 °C and salinities of 0.5–2.7 wt% NaCl equivalent.

Stage IV: Only VL-type FIs were observed in late-stage quartz crystals. The VL-type FIs from this stage homogenize to the liquid phase with T_h of 139–185 °C, T_{m-ice} of -2.6 to -0.9 °C and corresponding salinities of 1.6–4.2 wt% NaCl equivalent.

Laser Raman analyses of the representative FIs in the mineralized quartz from different stages indicate that the vapour phase primarily consists of H₂O (Fig. 7). Gaseous H₂O (3475 cm^{-1}) and small amounts of CO₂ (1231 cm^{-1}) were detected in the LV-type FIs during stage I (Fig. 7a), whereas the LV-type FIs from stage II and the VL-type FIs from stage III only have gaseous H₂O peaks near 3475 cm^{-1} (Fig. 7b, c).

5.c. Isotope analysis

5.c.1. H-O isotopes

Hydrogen and oxygen isotopic data for the quartz samples are listed in Table 2 and plotted in Figure 8. Ten samples have $\delta^{18}\text{O}_{V-SMOW}$ values of -2.7 to 9.2% , whereas the FI waters extracted from the quartz have δD_{SMOW} values ranging from -132.7 to -110.2% . The $\delta^{18}\text{O}_{\text{H}_2\text{O}}$ values of the hydrothermal

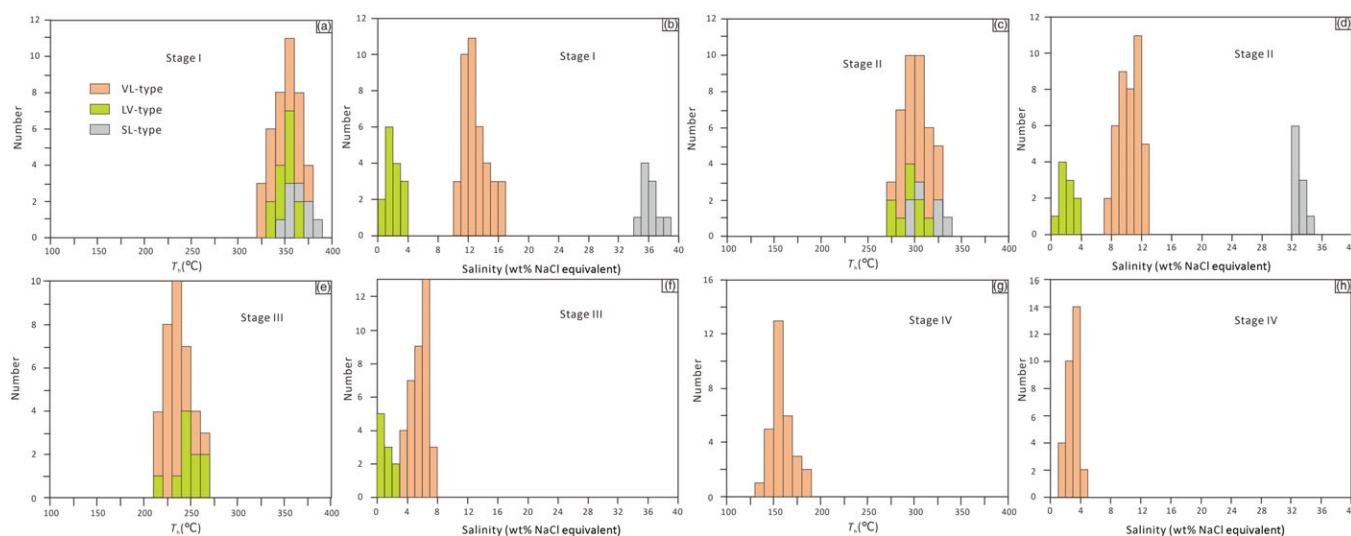


Fig. 6. (Colour online) Histograms of homogenization temperatures and salinities of FIs in different mineralization stages for the Cu–Pb–Zn mineralization at Panjiaduan.

fluids were calculated using the quartz–water isotopic fractionation equation $1000 \ln \alpha_{Qtz-H_2O} = (3.38 \times 10^6)/T^2 - 3.40$ (Clayton *et al.* 1972), in which T was determined based on the minimum T_h of the FIs from different stages. The calculated ore–fluid $\delta^{18}O_{H_2O}$ values are -1.1 to 2.6‰ (stage I), -5.6 to -3.9‰ (stage II), -14.3 to -11.4‰ (stage III) and -15.7‰ (stage IV).

5.c.2. He–Ar isotopes

The He and Ar isotopic analysis results from the FIs in the pyrite from stages II and III are listed in Table 3 and plotted in Figure 9. The ^4He and ^{40}Ar concentrations in the FIs range from 8.94×10^{-6} to $8.99 \times 10^{-6} \text{ cm}^3 \text{ STP g}^{-1}$ and 5.82×10^{-7} to $9.64 \times 10^{-7} \text{ cm}^3 \text{ STP g}^{-1}$, respectively. The $^3\text{He}/^4\text{He}$, $^{40}\text{Ar}/^{36}\text{Ar}$, $^3\text{He}/^{36}\text{Ar}$ and $^{40}\text{Ar}^*/^4\text{He}$ ratios are 0.032–0.052 Ra, 299–317, 1.88×10^{-4} to 2.08×10^{-4} and 1.66×10^{-3} to 6.68×10^{-3} , respectively, where Ra ($= 1.4 \times 10^{-6}$) represents the atmospheric $^3\text{He}/^4\text{He}$ ratio (Stuart *et al.* 1995). The $F^4\text{He}$ value, defined as the $^3\text{He}/^4\text{He}$ ratios of the samples relative to that of the atmosphere (0.1655; Kendrick *et al.* 2001), varies from 17 645 to 27 829. The proportion of radiogenic ^{40}Ar ($^{40}\text{Ar}^*$) ranges from 0.84 to 6.19, using the formula $^{40}\text{Ar}^*(\%) = \{1 - [295.5 / (^{40}\text{Ar}/^{36}\text{Ar})_{\text{sample}}]\} \times 100$.

6. Discussion

6.a. Source of the ore-forming fluids

6.a.1. H–O isotopic fingerprinting

The calculated $\delta^{18}O_{H_2O}$ (-15.7 to 2.6‰) and δD_{SMOW} (-132.7 to -110.2‰) values for the quartz from the four hydrothermal stages show a shift towards isotopic depletion from stage I to IV as shown in Table 2 and Figure 8, the latter of which is a plot of δD_{SMOW} versus $\delta^{18}O_{H_2O}$. The $\delta^{18}O_{H_2O}$ values for stage I (-1.1 to 2.6‰) are closer to those of magmatic water (7 – 9‰ ; Hedenquist & Lowenstern, 1994) but are significantly greater than those for a late Mesozoic meteoric water (-18‰ ; Zhang, 1989), indicating an initial magmatic water contribution to the ore-forming fluids. Since the local meteoric water generally has much lower $\delta^{18}O_{H_2O}$ values relative to the ore fluids, the calculated $\delta^{18}O_{H_2O}$ values (-15.7 to -3.9‰) from stages II–IV are negative. The δD_{SMOW} values ranging from -132.7 to -110.2‰ are significantly lower than those of

magmatic water (-50 to -85‰ ; Barnes, 1979). The depletion in the δD_{SMOW} values of the ore-forming fluids may have been produced by (1) changes in the oxygen fugacity of the fluids during deposition (Taylor, 1974), (2) hydrogen isotope fractionation between water and some reduced species (e.g. CH_4 and H_2), (3) boiling of the fluids (Koděra *et al.* 2005), (4) magma degassing resulting from mixing with meteoric waters (Rye & Ohmoto, 1974), and (5) the presence of secondary inclusions that may record fluid conditions different from the primary inclusions measured here. The effect of the first two processes is generally negligible in natural hydrothermal systems due to the large volume of H_2O (Taylor, 1974). Based on the above FI petrography and microthermometry, we speculate that fluid boiling and mixing with meteoric waters may be a more plausible explanation for the low δD_{SMOW} values exhibited in hydrothermal quartz in the Panjiaduan deposit. In addition, the measured low T_h and salinities of stage IV FIs suggest a significant involvement of meteoric waters in the fluid system (Fig. 6). Stage IV fluids have T_h of 139 – 185 °C, which is slightly higher than those of secondary inclusions at this stage and overlaps the purported range of decrepitation temperatures (100 – 200 °C) for secondary inclusions. The presence of fluids from secondary inclusions may therefore have an impact on the O and H isotope values of stage IV fluids. However, the proportion of primary inclusions in stage IV is up to 85%, indicating that the impact was likely insignificant.

Based on the techniques of Ohmoto & Rye (1974) and Field & Fifarek (1985), the isotopic compositions of the ore-forming fluids for the Cu–Pb–Zn veins in the Panjiaduan deposit have been modelled here in terms of exchange between water (e.g. magmatic and meteoric water) and igneous rocks (e.g. granodiorite and volcanic rocks from the Manitu Formation), as well as the temperature of equilibration. The isotopic compositions were calculated at water:rock ratios of 0.001, 0.01, 0.1, 1, 10 and 100 and equilibrium temperatures of 100, 200, 300 and 400 °C. The results of the computations, depicted in Figure 8, illustrate the systematics of isotopic exchange between magmatic or meteoric and rocks of igneous-hosted vein-type deposits. The isotopic compositions of the ore-forming fluids associated with these igneous-hosted vein-type deposits indicate that these fluids were probably mixed magmatic–meteoric waters similar to those reported from the

Table 1. Fluid-inclusion microthermometric data and calculated parameters of the Cu–Pb–Zn veins at Panjiaduan. T_e – eutectic temperature; T_{m-ice} – ice-melting temperature; T_{halite} – halite dissolution temperature; T_h – homogenization temperature; p – primary fluid inclusions; ps – pseudosecondary inclusions; s – secondary inclusions.

Sample no.	Stage	Type	Daughter minerals	n	Vapour bubble (vol%)	T_e (°C)	T_{m-ice} (°C)	T_{halite} (°C)	T_h (°C)	Salinity (wt% NaCl equivalent)
PJD-5-8	I	SL, p	Halite	10	10–25			251–298	348–386	34.7–38
PJD-5-7	I	VL, p		15	15–30		–11.4 to –7.0		335–372	10.5–15.4
PJD-5-7	I	VL, s		7	5–10				113–169	
PJD-5-8	I	VL, ps		4	15–20		–8.9 to –7.5		330–347	11.1–12.7
PJD-5-8	I	VL, p		11	15–30	–26.7 to –28.9	–12.1 to –7.6		324–380	11.2–16.1
PJD-5-8	I	VL, s		6	5–10				108–175	
PJD-5-9	I	VL, p		10	10–25	–27.3 to –29.5	–11.2 to –7.0		357–378	10.5–15.2
PJD-5-9	I	VL, s		4	5–10				127–153	
PJD-5-7	I	LV, p		5	80–85		–0.7 to –0.4		337–350	0.7–1.2
PJD-5-8	I	LV, p		4	75–80		–1.9 to –0.9		338–349	1.6–3.2
PJD-5-9	I	LV, p		6	75–85		–1.1 to –1.9		356–365	1.9–3.2
PJD-5-10	II	SL, p	Halite	6	10–20			210–245	283–332	32.4–34.4
PJD-5-11	II	SL, p	Halite	4	5–15			222–250	300–334	33.0–34.7
PJD-5-11	II	VL, p		27	10–20	–26.9 to –27.7	–8.9 to –6.0		295–330	9.2–12.8
PJD-5-10	II	VL, p		12	15–20		–7.9 to –5.0		278–296	7.9–11.2
PJD-5-10	II	VL, ps		5	10–20		–6.8 to –5.4		280–293	8.4–10.2
PJD-5-10	II	VL, s		4	5–10				109–164	
PJD-5-10	II	LV, p		6	70–75		–1.8 to –0.5		289–319	0.9–3.1
PJD-5-11	II	LV, p		3	75–80		–1.5 to –0.8		276–288	1.4–2.5
PJD-5-12	III	VL, p		22	10–20		–4.5 to –2		228–265	3.4–7.2
PJD-5-12	III	VL, ps		4	10–15		–3.9 to –2.4		219–238	4.0–6.3
PJD-5-13	III	VL, p		10	10–15	–27.7 to –28.5	–4.1 to –2.2		216–242	3.7–6.6
PJD-5-13	III	VL, s		5	5–10				109–148	
PJD-5-12	III	LV, p		7	70–75		–1.6 to –0.3		238–269	0.5–2.7
PJD-5-13	III	LV, p		6	70–75		–0.6 to –0.3		210–244	0.5–1.0
PJD-5-14	IV	VL, p		16	10–15		–2.6 to –1.9		147–185	3.2–4.2
PJD-5-15	IV	VL, p		14	10–15	–26.2 to –29	–2.0 to –0.9		139–177	1.6–3.4
PJD-5-15	IV	VL, s		8	5–10				103–129	

Guanajuato Cu–Pb–Zn–(Ag–Au) and Koru-Tesbihdere Pb–Zn–Cu–(Ag–Au) deposits (Mango *et al.* 2014; Cicek & Oyman, 2016), or predominantly meteoric water as is the case for the Shuangjianzishan Ag–Pb–Zn, Weilasituo Zn–Cu–Ag and Bairendaba Ag–Pb–Zn deposits (Ouyang *et al.* 2014; Li *et al.* 2017; Zhang *et al.* 2019). However, a minor component of magmatic water cannot be precluded on the basis of the smaller isotopic fractionation factors between water and rocks in partial equilibrium systems (Ohmoto & Rye, 1974), and the above causes for depleted the δD_{SMOW} values. The ore-forming fluids for the Cu–Pb–Zn veins at Panjiaduan are isotopically depleted relative to magmatic water or evolved magmatic water, but they are isotopically similar to meteoric water (Fig. 8). Because most mineral–H₂O fractionation factors are negative for hydrogen, magmatic fluid will not be isotopically depleted in deuterium through equilibration with the surrounding rock (Field & Fifarek, 1985). Consequently, we suggest that the ore-forming

fluids for the Cu–Pb–Zn veins in the Panjiaduan deposit are predominantly meteoric water that evolved from magmatic fluids.

6.a.2. He–Ar isotopic fingerprinting

As the most suitable mineral for trapping noble gases, the He and Ar isotopic compositions of the inclusion-trapped fluids within pyrite were not extensively lost within *c.* 100 Ma (Baptiste & Fouquet, 1996). Given that the Panjiaduan deposit has a sphalerite Rb–Sr age of 137 ± 5 Ma (Sun *et al.* 2021), the loss of trapped He and Ar isotopes is relatively limited and the $^3\text{He}/^4\text{He}$ and $^{40}\text{Ar}/^{36}\text{Ar}$ ratios are constant (Baptiste & Fouquet, 1996; Ballentine & Burnard, 2002). As pyrite samples were collected from drill holes, the influence of cosmogenic ^3He can therefore be eliminated (Simmons *et al.* 1987; Stuart *et al.* 1995). Because of the fact that pyrite is not a Li-bearing mineral as well, and that ^4He and ^{36}Ar from the nuclear decay of low concentrations of U and Th within the lattice of pyrite cannot diffuse into the trapped FIs (Stuart &

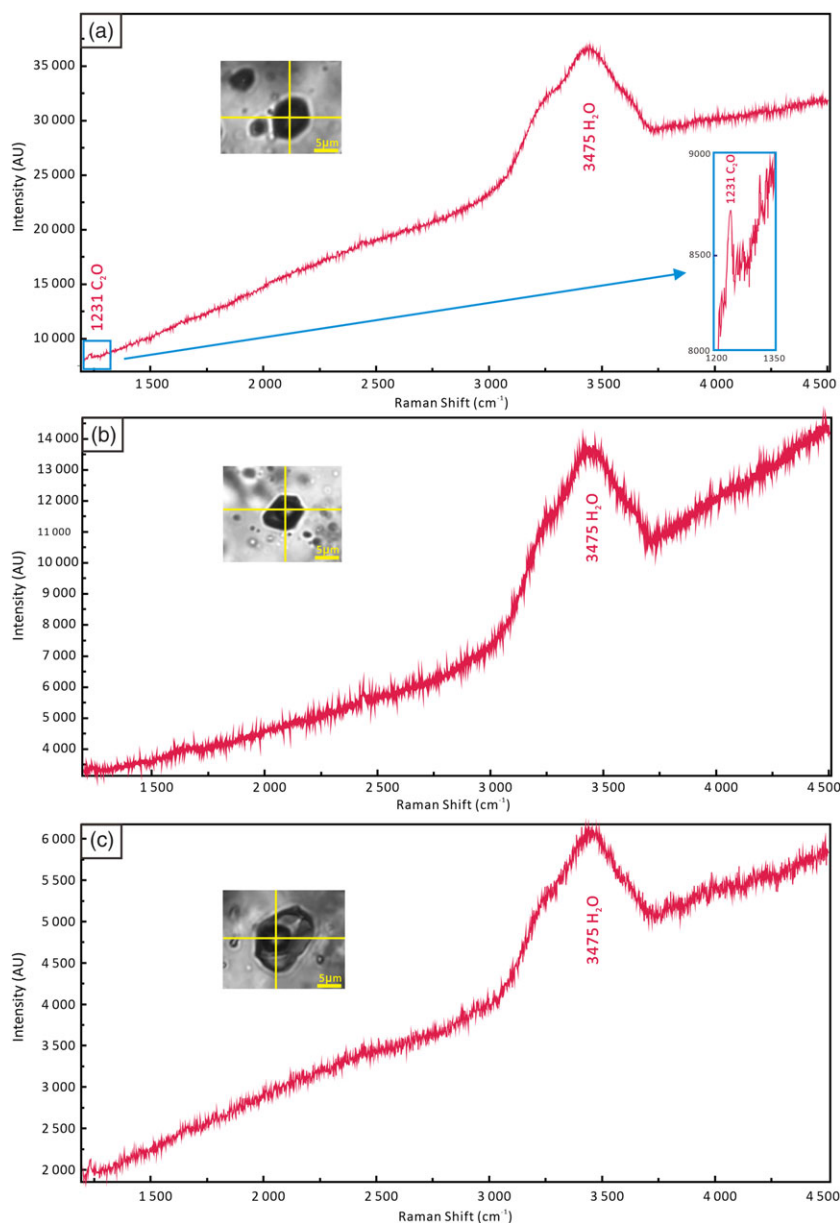


Fig. 7. (Colour online) Laser Raman spectra of FIs: (a) minor CO₂ in vapour phase of stage I vapour-rich LV-type inclusion; (b) H₂O in vapour phase of stage II vapour-rich LV-type inclusion; and (c) H₂O in vapour phase of stage II liquid-rich VL-type inclusion.

Turner, 1992; Ballentine & Burnard, 2002), the *in situ* production of radiogenic ⁴He and ³⁶Ar from the nuclear decay of dissolved U, Th and Li within pyrite is negligible. Noble gases in inclusion-trapped fluids have three possible sources: pure air-saturated water (ASW) with ³He/⁴He = 1.4 × 10⁻⁶ Ra and ⁴⁰Ar/³⁶Ar = 295.5, crust-derived fluids with ³He/⁴He = 0.01–0.05 Ra and ⁴⁰Ar/³⁶Ar ratios of > 45 000, and mantle-derived fluids with ³He/⁴He = 6–9 Ra and ⁴⁰Ar/³⁶Ar ratios of > 40 000 (Burnard *et al.* 1999).

In this study, the ³He/⁴He ratios of the FIs in pyrite range from 0.03 to 0.05 Ra, which are consistent with crust-derived ³He/⁴He values (0.01–0.05 Ra; Turner *et al.* 1993) and much lower than that of mantle values (6–9 Ra; Dunai & Baur, 1995). The F⁴He values (17 645–27 829), defined as the ⁴He/³⁶Ar ratio of a sample to the atmospheric ⁴He/³⁶Ar ratio of 0.1655, are more than 60 000 times the ASW concentration (F⁴He = 0.18–0.28; Kendrick *et al.* 2001). Moreover, the range of ³He/³⁶Ar ratios of 1.86 × 10⁻⁴ to 2.08 × 10⁻⁴ is much higher than similar ASW and atmospheric values (5 × 10⁻⁸; Turner *et al.* 1993; Stuart *et al.* 1995; Burnard *et al.* 1999).

This suggests that the involvement of He from ASW and the atmosphere are insignificant. As shown in Figure 9b, the ore-forming fluids contain a mixed He source of crust and ASW, but the mantle-derived He is negligible with He_{mantle} (%) = 0.19–0.50%, based on the equation from Anderson (2000). In a plot of ³He versus ⁴He (Fig. 9a), all samples plot in the crustal helium field. In summary, the characteristics of the He isotopic compositions indicate a predominantly crustal signature with minor contributions from ASW.

The measured ⁴⁰Ar/³⁶Ar ratio of the FIs in pyrite range from 299 to 317, which is higher than the atmospheric value of 295.5 but significantly lower than those of either the crust or mantle values. The ⁴⁰Ar*/⁴He ratios (1.66 × 10⁻³ to 6.68 × 10⁻³) of the analysed samples are distinctly lower than crustal values (0.2; Stuart *et al.* 1995; Fig. 9c), which can be attributed to the preferential acquisition of ⁴He over ⁴⁰Ar from aquifer rocks on the basis of the higher closure temperature of Ar (250 °C) relative to He (< 200 °C) in most sulphides (Lippolt & Weigel, 1988;

Table 2. Hydrogen and oxygen isotopic data of FIs in quartz from the Panjiaduan Cu–Pb–Zn deposit

Sample no.	Mineralized stages	Mineral	$\delta^{18}\text{O}_{\text{V-SMOW}}$ (‰)	δD (‰)	T (°C)	$\delta^{18}\text{O}_{\text{H}_2\text{O}}$ (‰)
PJD-1-1	Quartz-pyrite-arsenopyrite	Quartz	5.5	−111.5	324	−1.1
PJD-1-2	Quartz-pyrite-arsenopyrite	Quartz	6.1	−110.2	324	−0.5
PJD-1-3	Quartz-pyrite-arsenopyrite	Quartz	9.2	−121.1	324	2.6
PJD-2-1	Quartz-polymetallic sulphide	Quartz	2.7	−111.4	276	−5.6
PJD-2-2	Quartz-polymetallic sulphide	Quartz	4.4	−119.8	276	−3.9
PJD-2-3	Quartz-polymetallic sulphide	Quartz	3.5	−121.4	276	−4.8
PJD-3-1	Quartz-galena-sphalerite-argentite	Quartz	−2.7	−122.7	210	−14.3
PJD-3-2	Quartz-galena-sphalerite-argentite	Quartz	−1.3	−118.5	210	−12.9
PJD-3-3	Quartz-galena-sphalerite-argentite	Quartz	0.2	−120.4	210	−11.4
PJD-4-1	Quartz-calcite-minor sulphide	Quartz	1.3	−132.7	139	−15.7

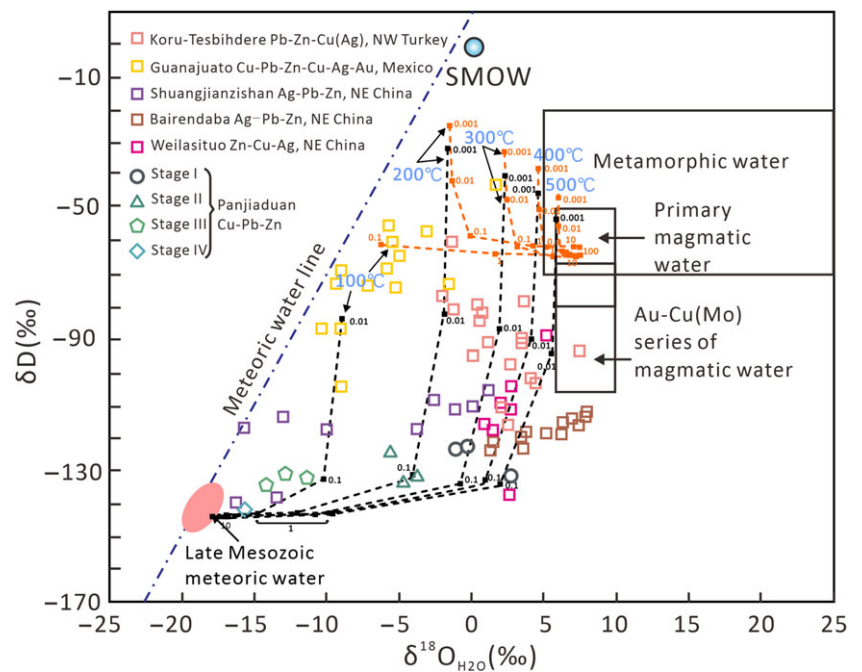


Fig. 8. (Colour online) δD versus $\delta^{18}\text{O}_{\text{H}_2\text{O}}$ plot of ore-forming fluids of the Panjiaduan deposit, after Taylor (1974). Source of the reference composition fields: Au–Cu(Mo) series of magmatic water from Zhang (1985), meteoric water line from Hoefs (2009). δD versus $\delta^{18}\text{O}_{\text{H}_2\text{O}}$ compositions of the Koru-Tesbihdere, Guanajuato, Shuangjianzishan, Weilasituo and Bairendaba deposits are from Mango *et al.* (2014), Cicek & Oyman (2016), Zhang *et al.* (2019), Ouyang *et al.* (2014) and Li *et al.* (2017), respectively.

Torgersen *et al.* 1988; Elliot *et al.* 1993; Ballentine & Burnard, 2002). To estimate the maximum $^{40}\text{Ar}/^{36}\text{Ar}$ proportion from the crust or mantle fluids, the maximum $^{40}\text{Ar}^*$ (%) for the Panjiaduan deposit is 6.19, using the equation of Kendrick *et al.* (2001). This result indicates that the $^{40}\text{Ar}/^{36}\text{Ar}$ values are consistent with a crustal source of fluid and that mantle-derived fluids provide only a minimal contribution to the ore-forming fluids. In a plot of R/Ra versus $^{40}\text{Ar}/^{36}\text{Ar}$ (Fig. 9b), all data points are near the trend line of the modified ASW (MASW; Stuart *et al.* 1995), indicating the incursion of meteoric waters. The Ar isotopic compositions are compatible with the primary signatures of most shallow meteoric waters (Elliot *et al.* 1993). In summary, the isotope data support the concept that the fluids entrapped in pyrite, which exhibit characteristics of near-atmospheric Ar and crustal He, may be a mixture of principally crust-derived fluids and meteoric waters with a negligible amount of mantle-derived fluids. Some published He–Ar isotopic compositions of typical Pb–Zn (Cu–Ag) vein-type deposits from around the world were also compiled in this study,

including the Iheya Pb–Zn (Cu), Lishan Pb–Zn–Cu and Tighza-Jbel Aouam Pb–Zn–Ag–(Cu) deposits (Rossi *et al.* 2017; Yang *et al.* 2021; Yu *et al.* 2021). The isotopic compositions from these deposits indicate that the ore-forming fluids were also predominantly a mixture of mantle-/crust-derived fluids and meteoric waters (Fig. 9).

6.b. Fluid-trapping pressure and mineralization depth

The trapping pressure can be estimated only when the trapping temperature is known or the FIs are trapped under immiscible/boiling conditions (Roedder & Bodnar, 1980; Brown & Hagemann, 1995). Fluid boiling can be inferred from the FI assemblages in stages I–III (Roedder, 1984), which have similar T_h but contrasting salinities and homogenization temperature paths (see Section 5.2). Although there are small amounts of CO_2 in stage I LV-type FIs, as demonstrated by laser Raman spectroscopy, the volatile content of FIs is dominated by

Table 3. Helium and argon isotopic compositions of Fls in pyrite from the Panjiaduan Cu–Pb–Zn deposit

Sample	Mineralized stages	Mineral	^4He (10^{-6} cm 3 STP/g)	$^3\text{He}/^4\text{He}$ (10^{-6})	R/Ra (10^{-2})	^{40}Ar (10^{-7} cm 3 STP/g)	$^{40}\text{Ar}/^{36}\text{Ar}$	$^3\text{He}/^{36}\text{Ar}$ (10^{-4})	$^{40}\text{Ar}^*$ (%)	$^{40}\text{Ar}^*/^4\text{He}$ (10^{-3})	F ^4He	$^4\text{He}_{\text{mantle}}$ (%)
PJD-6-1	Quartz-polymetallic sulphide	Pyrite	8.98	4.78	3.41	6.91	302	1.88	2.15	1.66	23 705	0.22
PJD-6-2	Quartz-polymetallic sulphide	Pyrite	8.96	6.81	4.86	9.01	308	2.08	4.06	4.08	18 497	0.44
PJD-6-3	Quartz-galena-sphalerite-argentite	Pyrite	8.99	4.49	3.21	5.82	299	1.88	0.84	5.43	27 829	0.19
PJD-6-4	Quartz-galena-sphalerite-argentite	Pyrite	8.94	7.31	5.22	9.64	317	1.86	6.19	6.68	17 645	0.5

$^{40}\text{Ar}^*$ (%) (the proportion of radiogenic ^{40}Ar) = $[1 - (295.5 / (^{40}\text{Ar}/^{36}\text{Ar})_{\text{sample}})] \times 100$; $^{40}\text{Ar}^*/^4\text{He}$ = $[(^{40}\text{Ar} - 295.5) \times ^{36}\text{Ar}] / ^4\text{He}$; R/Ra = $(^3\text{He}/^4\text{He})_{\text{sample}} / (^3\text{He}/^4\text{He})_{\text{air}}$, where $(^3\text{He}/^4\text{He})_{\text{air}} = 1.4 \times 10^{-6}$; F ^4He = $(^4\text{He}/^{36}\text{Ar})_{\text{sample}} / (^4\text{He}/^{36}\text{Ar})_{\text{air}}$, where $(^4\text{He}/^{36}\text{Ar})_{\text{air}} = 0.1655$ (Kendrick *et al.* 2001).

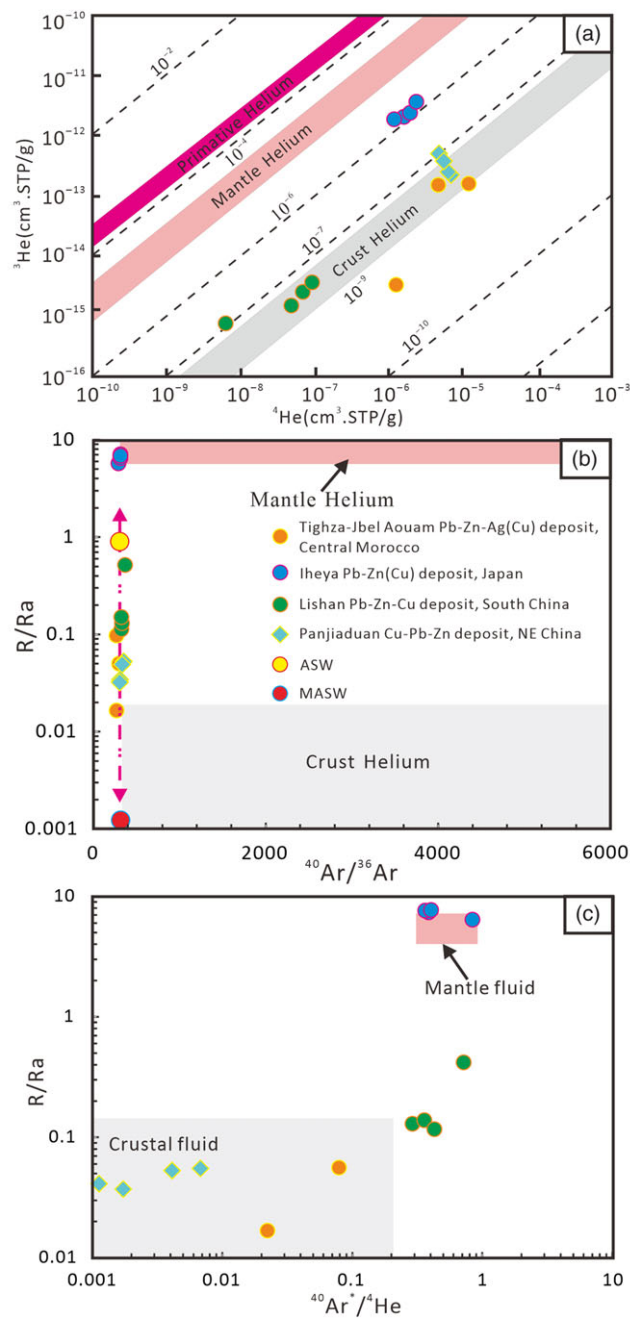


Fig. 9. (Colour online) (a) ^3He versus ^4He , (b) R/Ra versus $^{40}\text{Ar}/^{36}\text{Ar}$ and (c) R/Ra versus $^{40}\text{Ar}^*/^4\text{He}$ plots of inclusion-trapped fluids in pyrite from the Panjiaduan Cu–Pb–Zn deposit (modified from Mamyrin & Tolstikhin, 1984). The He–Ar isotopic compositions of typical Pb–Zn polymetallic vein-type deposits including the Tighza-Jbel Aouam, Iheya and Lishan deposits are from Yang *et al.* (2021), Rossi *et al.* (2017) and Yu *et al.* (2021), respectively.

H $_2$ O, and the daughter mineral is halite as subhedral/euhedral cubes. The evolution of the hydrothermal fluids can therefore be evaluated using the system NaCl–H $_2$ O. Following the isobar equations for a simple NaCl–H $_2$ O system provided by Driesner & Heinrich (2007), the estimated pressures are approximately 150–200 bar (stage I), 80–120 bar (stage II) and c. 50 bar (stage III) (Fig. 10), which correspond to depths of 1.5–2.0 km, 0.8–1.2 km and c. 0.5 km, respectively, assuming hydrostatic conditions.

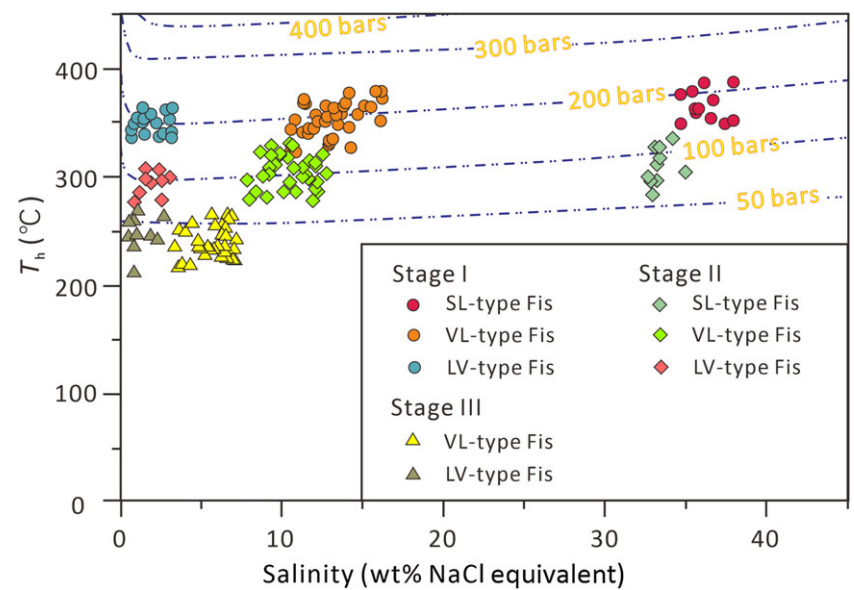


Fig. 10. (Colour online) Pressure estimation for FIs of the Panjiaduan Cu–Pb–Zn deposits. Isobars were calculated from the equations of Driesner & Heinrich (2007).

6.c. Fluid evolution and ore precipitation

Based on FI microthermometry and laser Raman spectroscopy, the ore-forming fluids that created the Cu–Pb–Zn veins in the Panjiaduan deposit evolved from a high- to medium-temperature and high- to moderate-salinity NaCl–H₂O–(CO₂) fluid during stage I to a moderate- to low-temperature and low-salinity NaCl–H₂O fluid during stage IV. Fluid boiling induced by the sudden pressure release during upwards migration of the ore-forming fluid was one of the dominant ore-forming mechanisms for base metal vein deposits (e.g. Canet *et al.* 2011; Moncada *et al.* 2012; Kouhestani *et al.* 2019; Fan *et al.* 2021). This process could have effectively led to degassing of CO₂, increasing pH conditions and sulphur fugacity (by increasing the H₂S solubility), and decreasing oxygen fugacity of the ore-forming fluids (Hedenquist & Henley, 1985; Simmons & Christenson, 1994). Minor dissolved CO₂ in the laser Raman spectroscopy of the stage I LV-type FIs and predominant gaseous H₂O of stages II–III LV-type FIs are consistent with the degassing of CO₂ (Fig. 7).

The boiling fluid likely produced hydrofracturing of the overlying and surrounding wall rocks in the granodiorite and Manitu Formation, and it could also have further accelerated the influx and circulation of meteoric waters. The decreasing homogenization temperatures and their positive correlation with salinity from stage I to IV imply an inflow of meteoric waters that mixed with the early magmatic fluids (Simmons *et al.* 2005; Fig. 6), a conclusion that is supported by the H–O–He–Ar isotope data (see Section 6.1, Figs 8, 9). The mixing of magmatic and meteoric fluids would also change the fluid pH and oxygen fugacity (O’Neil & Silberman, 1974), and can also result in the deposition of Pb–Zn polymetallic veins (e.g. Fusswinkel *et al.* 2013; Mango *et al.* 2014; Ouyang *et al.* 2014; Cicek & Oyman, 2016; Desanois *et al.* 2019). Along with meteoric water input and fluid cooling, the temperature and salinity of the fluids were reduced and no SL-type FIs are observed in stage III. The H–O isotope data for stage IV fluids are close to the meteoric water line, indicating that the magmatic fluid component became negligible with the continuous input of meteoric waters. The stage IV fluid is characterized by low temperature and salinity coupled with an increase in the oxygen fugacity and acidity as indicated by the change in the stage IV mineralogy

(i.e. quartz, chlorite, epidote, carbonate and minor sulphide). Additionally, fluid–rock reactions could have been locally important and partially manifested by the well developed hydrothermal alteration around the base metal veins. In summary, hydrothermal fluid boiling, cooling, mixing with meteoric waters and fluid–rock reactions are advocated as important mechanisms that contributed to the Cu–Pb–Zn vein formation.

6.d. Ore genesis

The SGXR hosts several Cu–Pb–Zn–Ag vein-type deposits. They are all genetically related to Early Cretaceous magmatism (140–133 Ma; Zeng *et al.* 2012; Ouyang *et al.* 2013), which was temporally coeval with the formation of nearby porphyry Mo–(Cu) and skarn Fe–Sn–Pb–Zn deposits (e.g. the Hashitu Mo, Aolunhua Mo–Cu, Huanggang Sn–Fe and Haobugao Fe–Zn deposits; Wu *et al.* 2011b; Mei *et al.* 2015; Zhai *et al.* 2018a; Shu *et al.* 2020). However, except for the Cu–Pb–Zn veins in the Panjiaduan deposit, there is also porphyry Mo mineralization hosted in the syenogranite as veinlet-disseminated sulphide ores (Mo grade up to 0.33%) in the northwestern part of the Panjiaduan deposit. The spatial relationship of porphyry Mo mineralization to polymetallic vein mineralization may suggest that there is a genetic relationship between the two ore types. However, published geochronological data show that the porphyry Mo mineralization at Panjiaduan formed during Late Triassic time and is probably genetically related to the syenogranite (zircon U–Pb: 236.1–233.9 Ma), while the vein-type Cu–Pb–Zn mineralization occurred during Early Cretaceous time (sphalerite Rb–Sr: 138.5 ± 3.5 Ma) (Sun *et al.* 2021). We therefore propose that there are two magmatic-hydrothermal events (Late Triassic Mo and Early Cretaceous Cu–Pb–Zn) at Panjiaduan, and that no direct genetic link occurs between the two ore types. The Late Triassic porphyry Mo mineralization formed in a post-collision extensional setting following the Palaeo-Asian Ocean closure (Sun *et al.* 2021). The Early Cretaceous SGXR and the northeastern part of China were dominated by an extensional setting related to lithospheric thinning and asthenospheric upwelling, which was caused by the Palaeo-Pacific subduction rollback (Fig. 11; Wu *et al.* 2007;

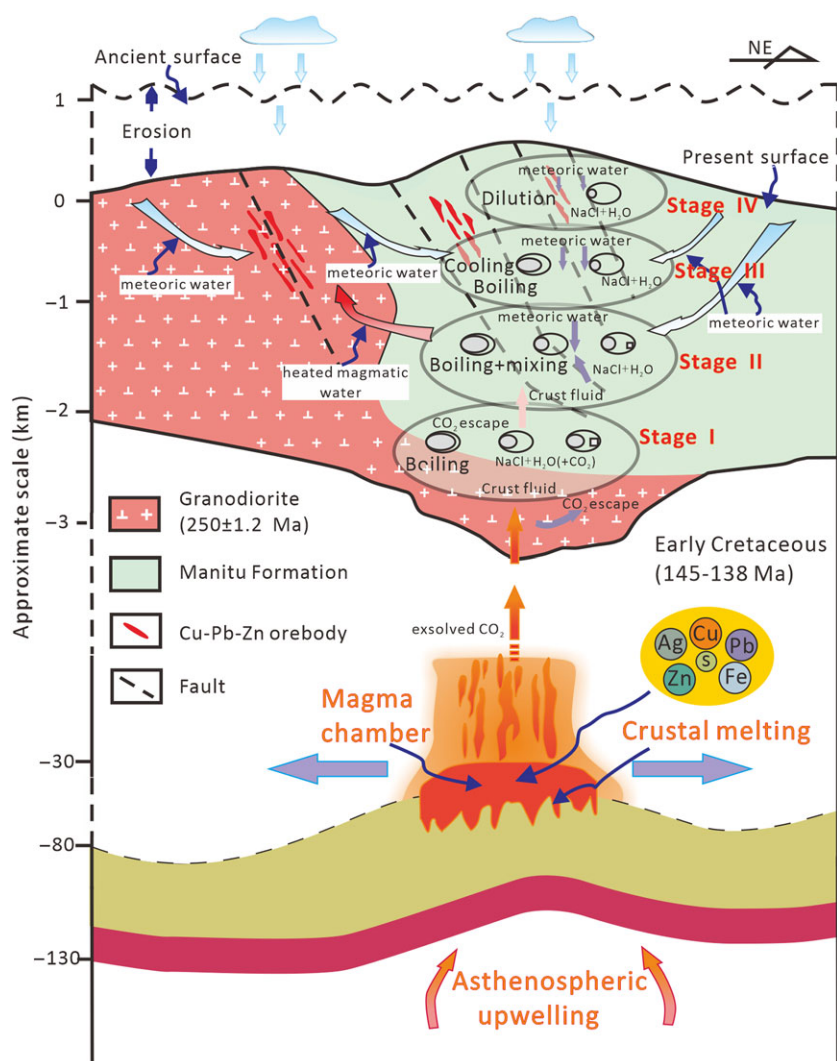


Fig. 11. (Colour online) Genetic model for the Panjiaduan Cu-Pb-Zn deposit.

Kiminami & Imaoka, 2013). The Early Cretaceous base metal veins in both the Panjiaduan deposit and the SGXR were therefore likely formed in an intracontinental extensional setting, which is favourable for partial melting of crustal rocks (Shu *et al.* 2016). The magmatic fluids migrated upwards into the host granodiorite and volcanic rocks of the Manitu Formation through widespread extensional faults in the district (Fig. 11), which led to a sudden pressure release because of a change from lithostatic to hydrostatic conditions and subsequent fluid boiling and fluid-rock reactions. In addition, structures spatially associated with sulphide mineralization may also have provided permeable conduits favourable for deep circulation of meteoric waters, which likely aided the mixing of magmatic fluids and meteoric waters. This relationship was previously documented for the Pb-Zn (Cu-Ag) veins of the Uchuchacua district in Peru (Bussell *et al.* 1990), the Guanajuato Cu-Pb-Zn (Ag-Au) deposit in Mexico (Mango *et al.* 2014) and the Koru-Tesbihdere Pb-Zn-Cu (Ag-Au) deposit in Turkey (Cicek & Oyman, 2016). A convecting hydrothermal system resulting from tectonomagmatic activities is therefore the key factor for

Pb-Zn polymetallic vein formation, which equilibrated over a wide range of temperatures and water:rock ratios.

7. Conclusion

1. The ore-forming fluids that created the Cu-Pb-Zn veins in the Panjiaduan deposit evolved from a high- to medium-temperature and a high- to moderate-salinity NaCl-H₂O-(CO₂) fluid system which changed to a moderate- to low-temperature and low-salinity NaCl-H₂O fluid system with time. The H-O isotope data indicate that the fluids were predominantly meteoric water but initially magmatic in origin.
2. The He and Ar isotopic compositions of FIs in pyrite from the Cu-Pb-Zn veins in the Panjiaduan deposit suggest that the ore-forming fluids were a mixture of principally crust-derived fluids and meteoric waters as well as negligible mantle-derived fluids.
3. Fluid boiling, cooling, mixing with meteoric waters, and fluid-rock reactions are advocated for as the primary mechanisms for Cu-Pb-Zn vein formation.

4. The Panjiadian Cu–Pb–Zn deposit is a hydrothermal vein ore system that is temporally and genetically related to large-scale Early Cretaceous magmatism.

Acknowledgements. The project was funded by the National Key R&D Program of China (2017YFC0601304) and the Opening Foundation of Key Laboratory of Mineral Resources Evaluation in Northeast Asia, Ministry of Land and Resources of China (DBY-ZZ-18-12, DBY-KY-18-08). The quality of the paper was markedly improved by the reviews and edits of Vasilios Melfos and associate editor Paul Spry.

References

- Anderson DL (2000) The statistics and distribution of helium in the mantle. *International Geology Review* **42**, 289–311.
- Ballentine CJ and Burnard PG (2002) Production, release and transport of noble gases in the continental crust. *Reviews in Mineralogy and Geochemistry* **47**, 481–538.
- Baptiste P and Fouquet Y (1996) Abundance and isotopic composition of helium in hydrothermal sulfides from the East Pacific Rise at 13 °N. *Geochimica et Cosmochimica Acta* **60**, 87–93.
- Barnes HL (1979) *Geochemistry of Hydrothermal Ore Deposits*. New York: Wiley, pp. 404–60.
- Brown PE and Hagemann SG (1995) MacFlincor and its application to fluids in Archean lode-gold deposits. *Geochimica et Cosmochimica Acta* **59**, 3943–52.
- Burnard PG, Hu RZ, Turner G and Bi XW (1999) Mantle, crustal and atmospheric noble gases in Ailaoshan gold deposits, Yunnan province, China. *Geochimica et Cosmochimica Acta* **63**, 1595–604.
- Bussell MA, Alpers CN, Petersen U, Shepherd TJ, Bermudez C and Baxter AN (1990) The Ag–Mn–Pb–Zn vein, replacement, and skarn deposits of Uchucchacua, Peru; studies of structure, mineralogy, metal zoning, Sr isotopes, and fluid inclusions. *Economic Geology* **85**, 1348–83.
- Canet C, Franco SI, Prol-Ledesma RM, González-Partida E and Villanueva-Estrada RE (2011) A model of boiling for fluid inclusion studies: application to the Bolaños Ag–Au–Pb–Zn epithermal deposit, Western Mexico. *Journal of Geochemical Exploration* **110**, 118–25.
- Chen YJ and Li N (2009) Nature of ore-fluids of intracontinental intrusion-related hypothermal deposits and its difference from those in island arcs. *Acta Petrologica Sinica* **25**, 2477–508.
- Chen YJ, Zhang C, Wang P, Pirajno F and Li N (2017) The Mo deposits of Northeast China: A powerful indicator of tectonic settings and associated evolutionary trends. *Ore Geology Reviews* **81**, 602–640.
- Cicek M and Oyman T (2016) Origin and evolution of hydrothermal fluids in epithermal Pb–Zn–Cu ± Au ± Ag deposits at Koru and Tesbihdere mining districts, Canakkale, Biga Peninsula, NW Turkey. *Ore Geology Reviews* **78**, 176–95.
- Clayton RN and Mayeda TK (1963) The use of bromine pentafluoride in the extraction of oxygen from oxides and silicates for isotopic analysis. *Geochimica et Cosmochimica Acta* **27**, 43–52.
- Clayton RN, O'Neil JR and Mayeda TK (1972) Oxygen isotope exchange between quartz and water. *Journal of Geophysical Research* **77**, 3057–67.
- Desanois L, Lüders V, Niedermann S and Trumbull RB (2019) Formation of epithermal Sn–Ag–(Zn) vein-type mineralization at the Pirquitas deposit, NW Argentina: fluid inclusion and noble gas isotopic constraints. *Chemical Geology* **508**, 78–91.
- Donskaya TV, Gladkochub DP, Mazukabzov AM and Ivanov AV (2013) Late Paleozoic–Mesozoic subduction-related magmatism at the southern margin of the Siberian continent and the 150 million year history of the Mongol–Okhotsk Ocean. *Journal of Asian Earth Sciences* **62**, 79–97.
- Driesner T and Heinrich CA (2007) The system H₂O–NaCl. Part I: Correlation formulae for phase relations in temperature–pressure–composition space from 0 to 1000°C, 0 to 5000 bar, and 0 to 1 XNaCl. *Geochimica et Cosmochimica Acta* **71**, 4880–901.
- Dunai TJ and Baur H (1995) Helium, neon and argon systematics of the European subcontinental mantle: implications for its geochemical evolution. *Geochimica et Cosmochimica Acta* **59**, 2767–84.
- Elliot T, Ballentine CJ, O'Nions RK and Ricchiuto T (1993) Carbon, helium, neon and argon isotopes in a Po basin natural gas field. *Chemical Geology* **106**, 429–40.
- Fan XZ, Sun FY, Xu CH, Xin W, Wang YC and Zhang Y (2021) Genesis of Harizha Ag–Pb–Zn deposit in the eastern Kunlun Orogen, NW China: Evidence of fluid inclusions and C–H–O–S–Pb isotopes. *Resource Geology* **71**, 177–201.
- Field CW and Fifarek RH (1985) Geology and geochemistry of epithermal systems. *Reviews in Economic Geology* **2**, 99–128.
- Fusswinkel T, Wagner T, Wälle M, Wenzel T, Heinrich CA and Markl G (2013) Fluid mixing forms basement-hosted Pb–Zn deposits; insight from metal and halogen geochemistry of individual fluid inclusions. *Geology* **41**, 679–82.
- Gao X, Zhou ZH, Breiter K, Ouyang HG and Liu J (2019) Ore-formation mechanism of the Weilasituo tin-polymetallic deposit, NE China: Constraints from bulk-rock and mica chemistry, He–Ar isotopes, and Re–Os dating. *Ore Geology Reviews* **109**, 163–83.
- Gu AL (2016) Study on the mineralization processes and metallogenic model of epithermal-porphyrty copper-polymetallic mineralization system in the central and eastern of Great Xing'an Range, China. Ph.D. thesis. Jilin University, Changchun. Published thesis (in Chinese with English abstract).
- Hedenquist JW and Henley RW (1985) The importance of CO₂ on freezing point measurements of fluid: evidence from active geothermal systems and implications for epithermal ore deposition. *Economic Geology* **80**, 1379–406.
- Hedenquist JW and Lowenstern JB (1994) The role of magmas in the formation of hydrothermal ore deposits. *Nature* **370**, 519–27.
- Hoefs J (2009) *Stable Isotope Geochemistry*. Berlin: Springer-Verlag.
- Kendrick MA, Burgess R, Patrick RAD and Turner G (2001) Fluid inclusion noble gas and halogen evidence on the origin of Cu-porphyrty mineralizing fluids. *Geochimica et Cosmochimica Acta* **65**, 2651–68.
- Kiminami K and Imaoka T (2013) Spatiotemporal variations of Jurassic–Cretaceous magmatism in eastern Asia (Tan-Lu fault to SW Japan): Evidence for flat-slab subduction and slab rollback. *Terra Nova* **25**, 414–22.
- Koděra P, Lexa J, Rankin AH and Fallick AE (2005) Epithermal gold veins in a caldera setting: Banská Hodruša, Slovakia. *Mineralium Deposita* **39**, 921–943.
- Kouhestani H, Mokhtari MAA, Qin KZ and Zhao JX (2019) Fluid inclusion and stable isotope constraints on ore genesis of the Zajkan epithermal base metal deposit, Tarom–Hashtjin metallogenic belt, NW Iran. *Ore Geology Reviews* **109**, 564–84.
- Li SD, Wang KY, Wang YC, Zhang XB and Quan HY (2017) Genesis of the Bairendaba Ag–Zn–Pb deposit, southern great Xing'an range, NE China: a fluid inclusion and stable isotope study. *Geofluids* **2017**, 1–18.
- Lippolt HJ and Weigel E (1988) ⁴He diffusion in Ar retentive minerals. *Geochimica et Cosmochimica Acta* **52**, 1449–58.
- Liu CH, Bagas L and Wang FX (2016a) Isotopic analysis of the super-large Shuangjianzishan Pb–Zn–Ag deposit in Inner Mongolia, China: constraints on magmatism, metallogenesis, and tectonic setting. *Ore Geology Reviews* **75**, 252–67.
- Liu JM, Zhang R and Zhang QZ (2004) The regional metallogeny of Da Hingan Ling, China. *Geoscience Frontiers* **1**, 269–77 (in Chinese).
- Liu Y, Jiang SH, Bagas L, Han N, Chen CL and Kang H (2017) Isotopic (C–O–S) geochemistry and Re–Os geochronology of the Haobugao Zn–Fe deposit in Inner Mongolia, NE China. *Ore Geology Reviews* **82**, 130–47.
- Liu YF, Jiang SH and Bagas L (2016b) The genesis of metal zonation in the Weilasituo and Bairendaba Ag–Zn–Pb–Cu–(Sn–W) deposits in the shallow part of a porphyry Sn–W–Rb system, Inner Mongolia, China. *Ore Geology Reviews* **75**, 150–73.
- Ma XL, Wang KY, Zhou HY, Li SD, Li J, Shi KT, Wang ZG, Yang H and Lai CK (2019) Genesis and tectonic setting of Shenshan Fe–Cu deposit in Inner Mongolia, Northeast China: constraints from geochemistry, U–Pb and Re–Os geochronology, and Hf isotopes. *Ore Geology Reviews* **112**, 103046.
- Mamyrin BA and Tolstikhin IN (1984) *Helium Isotopes in Nature*. Amsterdam: Elsevier, 273 p.
- Mango H, Arehart GB, Oreskes N and Zantop H (2014) Origin of epithermal Ag–Au–Cu–Pb–Zn mineralization in Guanajuato, Mexico. *Mineralium Deposita* **49**, 119–43.

- Mei W, Lü XB, Liu Z, Tang RK, Ai Z, Wang XD and Cisse M (2015) Geochronological and geochemical constraints on the ore-related granites in Huanggang deposit, Southern Great Xing'an Range, NE China and its tectonic significance. *Geosciences Journal* **19**, 53–67.
- Moncada D, Mutchler S, Nieto A, Reynolds TJ, Rimstidt JD and Bodnar RJ (2012) Mineral textures and fluid inclusion petrography of the epithermal Ag–Au deposits at Guanajuato, Mexico: application to exploration. *Journal of Geochemical Exploration* **114**, 20–35.
- O'Neil JR and Silberman ML (1974) Stable isotope relations in epithermal Au–Ag deposits. *Economic Geology* **69**, 902–9.
- Ohmoto H and Rye RO (1974) Hydrogen and oxygen isotopic compositions of fluid inclusions in the Kuroko deposits, Japan. *Economic Geology* **69**, 947–53.
- Ouyang HG, Mao JW and Santosh M (2013) Anatomy of a large Ag–Pb–Zn deposit in the Great Xing'an Range, northeast China: metallogeny associated with Early Cretaceous magmatism. *International Geology Review* **55**, 411–29.
- Ouyang HG, Mao JW, Santosh M, Wu Y, Hou L and Wang XF (2014) The Early Cretaceous Weilasituo Zn–Cu–Ag vein deposit in the southern Great Xing'an Range, northeast China: fluid inclusions, H, O, S, Pb isotope geochemistry and genetic implications. *Ore Geology Reviews* **56**, 503–15.
- Ouyang HG, Mao JW, Zhou ZH and Su HM (2015) Late Mesozoic metallogeny and intracratonic magmatism, southern Great Xing'an Range, northeastern China. *Gondwana Research* **27**, 1153–72.
- Robinson PT, Zhou MF, Hu XF, Reynolds P, Bai WJ and Yang JS (1999) Geochemical constraints on the origin of the Hegenshan Ophiolite, Inner Mongolia, China. *Journal of Asian Earth Sciences* **17**, 423–442.
- Roedder E (1984) *Fluid Inclusions*. Chantilly (VA): Mineralogical Society of America. Reviews in Mineralogy and Geochemistry, no. 12, 644 p.
- Roedder E and Bodnar RJ (1980) Geologic pressure determinations from fluid inclusion studies. *Annual Review of Earth and Planetary Sciences* **8**, 263–301.
- Rossi M, Gasquet D, Cheilietz A, Tarrieu L, Bounajma H, Mantoy T, Reisberg L, Deloule E, Boulvais P and Burnard P (2017) Isotopic and geochemical constraints on lead and fluid sources of the Pb–Zn–Ag mineralization in the polymetallic Tighza–Jbel Aouam district (Central Morocco), and relationships with the geodynamic context. *Journal of African Earth Sciences* **127**, 194–210.
- Rye RO and Ohmoto H (1974) Sulfur and carbon isotopes and ore genesis: a review. *Economic Geology* **69**, 826–842.
- Safonova IY and Santosh M (2014) Accretionary complexes in the Asia–Pacific region: tracing archives of ocean plate stratigraphy and tracking mantle plumes. *Gondwana Research* **25**, 126–58.
- Shi KT, Wang KY, Ma XL, Li SD, Li J and Wang R (2020) Fluid inclusions, C–H–O–S–Pb isotope systematics, geochronology and geochemistry of the Budunhua Cu deposit, northeast China: implications for ore genesis. *Geoscience Frontiers* **11**, 1145–61.
- Shu QH, Chang ZS, Lai Y, Zhou YT and Yan C (2016) Regional metallogeny of Mo-bearing deposits in northeastern China, with new Re–Os dates of porphyry Mo deposits in the northern Xilamulun district. *Economic Geology* **111**, 1783–98.
- Shu QH, Chang ZS and Mavrogenes J (2020) Fluid compositions reveal fluid nature, metal deposition mechanisms, and mineralization potential; an example at the Haobugao Zn–Pb skarn, China. *Geology* **49**, 473–7.
- Shu QH, Lai Y, Sun Y, Wang C and Meng S (2013) Ore genesis and hydrothermal evolution of the Baiyinnuo'er zinc–lead skarn deposit, northeast China: evidence from isotopes (S, Pb) and fluid inclusions. *Economic Geology* **108**, 835–60.
- Simmons SF and Christenson BW (1994) Origins of calcite in a boiling geothermal system. *American Journal of Science* **294**, 361–400.
- Simmons SF, Sawkins FJ and Schlutter DJ (1987) Mantle-derived helium in two Peruvian hydrothermal ore deposits. *Nature* **329**, 429–32.
- Simmons SF, White NC and John DA (2005) Geological characteristics of epithermal precious and base metal deposits. In *Economic Geology, One Hundredth Anniversary Volume* (eds JW Hedenquist, JFH Thompson, RJ Goldfarb and JP Richards), pp. 485–522. Littleton (CO): Society of Economic Geologists.
- Sorokin AA, Yarmolyuk VV, Kotov AB, Sorokin AP, Kudryashov NM and Li LY (2004) Geochronology of Triassic–Jurassic granitoids in the southern framing of the Mongol–Okhotsk foldbelt and the problem of Early Mesozoic granite formation in central and eastern Asia. *Doklady Earth Sciences* **399**, 1091–4.
- Sterner SM and Bodnar RJ (1984) Synthetic fluid inclusions in natural quartz. I. Compositional types synthesized and applications to experimental geochemistry. *Geochimica et Cosmochimica Acta* **48**, 2659–68.
- Stuart FM, Burnard PG, Taylor RP and Turner G (1995) Resolving mantle and crustal contributions to ancient hydrothermal fluids: He–Ar isotopes in fluid inclusions from Dae Hwa W–Mo mineralization, South Korea. *Geochimica et Cosmochimica Acta* **59**, 4663–73.
- Stuart FM and Turner G (1992) The abundance and isotopic composition of the noble gases in ancient fluids. *Chemical Geology* **101**, 97–109.
- Sun DY, Gou J, Ren YS, Fu CL, Wang X and Liu XM (2011) Zircon U–Pb dating and study on geochemistry of volcanic rocks in Manitu Formation from southern Manchuria, Inner Mongolia. *Acta Petrologica Sinica* **27**, 3083–94 (in Chinese with English abstract).
- Sun QF, Wang KY, Sun FY, Lai CK, Zhang M, Zhao CG and Sun LX (2021) Superimposing porphyry Mo and vein-type Cu–Pb–Zn mineralization in the Panjiaduan deposit, great Xing'an range (NE China): perspective from zircon U–Pb and sphalerite Rb–Sr dating, geochemistry and S–Pb isotopes. *Ore Geology Reviews* **139**, 104538.
- Tang WH, Li J, Wang KY, Li SD, Cai WY, Liu HL and Wang YC (2019) Ore genesis and tectonic setting of the Laojiagou porphyry molybdenum deposit, Inner Mongolia, China: evidence from geology, fluid inclusions, H–O isotopes, zircon U–Pb geochronology, and geochemistry. *Arabian Journal of Geosciences* **12**, 1–19.
- Taylor HP (1974) The application of oxygen and hydrogen isotope studies to problems of hydrothermal alteration and ore deposition. *Economic Geology* **69**, 843–83.
- Torgersen T, Kennedy BM and Hiyagon H (1988) Argon accumulation and the crustal degassing flux of ⁴⁰Ar in the Great Artesian Basin, Australia. *Earth and Planetary Science Letters* **92**, 43–56.
- Turner G, Burnard PG, Ford JL, Gilmour JD, Lyon IC and Stuart FM (1993) Tracing fluid sources and interaction. *Philosophical Transactions of the Royal Society of London* **344**, 127–40.
- Wang JB, Wang YW, Wang LJ and Uemoto T (2001) Tin–polymetallic mineralization in the southern part of the Da Hinggan Mountains, China. *Resource Geology* **51**, 283–91.
- Wang YW, Wang JB, Wang LJ and Chen YZ (2006) Tin mineralization in the Dajing tin–polymetallic deposit, Inner Mongolia, China. *Journal of Asian Earth Sciences* **28**, 320–31.
- Wilde SA (2015) Final amalgamation of the Central Asian Orogenic Belt in NE China: Paleo-Asian ocean closure versus Paleo-Pacific plate subduction – a review of the evidence. *Tectonophysics* **662**, 345–62.
- Wopenka B, Pasteris JD and Freeman JJ (1990) Analysis of individual fluid inclusions by Fourier transform infrared and Raman microspectroscopy. *Geochimica et Cosmochimica Acta* **54**, 519–33.
- Wu FY, Han RH, Yang JH, Wilde SA, Zhai MG and Park SC (2007) Initial constraints on the timing of granitic magmatism in North Korea using U–Pb zircon geochronology. *Chemical Geology* **238**, 232–48.
- Wu FY, Sun DY, Ge WC, Zhang YB, Grant ML, Wilde SA and Jahn BM (2011a) Geochronology of the Phanerozoic granitoids in northeastern China. *Journal of Asian Earth Sciences* **41**, 1–30.
- Wu HY, Zhang LC, Wan B, Chen ZG, Zhang XJ and Xiang P (2011b) Geochronological and geochemical constraints on Aolunhua porphyry Mo–Cu deposit, northeast China, and its tectonic significance. *Ore Geology Reviews* **43**, 78–91.
- Xiao WJ, Windley BF, Hao JJ and Zhai MG (2003) Accretion leading to collision and the Permian Solonker suture, Inner Mongolia, China: termination of the Central Asian Orogenic Belt. *Tectonics* **22**, 1–20.
- Xu WL, Pei FP, Wang F, Meng E, Ji WQ, Yang DB and Wang W (2013) Spatial-temporal relationships of Mesozoic volcanic rocks in NE China: constraints on tectonic overprinting and transformations between multiple tectonic regimes. *Journal of Asian Earth Sciences* **74**, 167–93.
- Yang H, Ma WL, Wang R, Ma XL and Wang KY (2020) Factors controlling deposition of metallic minerals in the Meng'entaolegai Ag–Pb–Zn deposit, Inner Mongolia, China: evidence from fluid inclusions, isotope systematics, and thermodynamic model. *Journal of Earth Science* **31**, 271–86.

- Yang ZF, Zhai SK, Yu ZH, Zhang X, Xu J and Su F** (2021) Fluid sources and precipitation mechanisms of Pb–Zn–(Cu) sulphide–sulphate in the Iheya North Knoll hydrothermal field, Okinawa Trough: insights from fluid inclusions, He and Ar isotopes. *International Geology Review* **63**, 1703–18.
- Yu DS, Xu DR, Wang ZL, Xu K, Huang QY, Zou SH, Zhao ZX and Deng T** (2021) Trace element geochemistry and O–S–Pb–He–Ar isotopic systematics of the Lishan Pb–Zn–Cu hydrothermal deposit, NE Hunan, South China. *Ore Geology Reviews* **133**, 104091.
- Zeng QD, Liu JM, Chu SX, Wang YB, Sun Y, Duan XX and Zhou LL** (2012) Mesozoic molybdenum deposits in the East Xingmeng orogenic belt, northeast China: characteristics and tectonic setting. *International Geology Review* **54**, 1843–69.
- Zeng QD, Liu JM, Yu CM, Ye J and Liu HT** (2011) Metal deposits in the Da Hinggan Mountains, NE China: style, characteristics, and exploration potential. *International Geology Review* **53**, 846–78.
- Zeng QD, Qin KZ, Liu JM, Li GM, Zhai MH, Chu SX and Guo YP** (2015) Porphyry molybdenum deposits in the Tianshan–Xingmeng orogenic belt, northern China. *International Journal of Earth Sciences* **104**, 991–1023.
- Zhai DG, Liu JJ, Tombros S and Williams-Jones AE** (2018a) The genesis of the Hashitu porphyry molybdenum deposit, Inner Mongolia, NE China: constraints from mineralogical, fluid inclusion, and multiple isotope (H, O, S, Mo, Pb) studies. *Mineralium Deposita* **53**, 377–97.
- Zhai DG, Liu JJ, Zhang AL and Sun YQ** (2017) U–Pb, Re–Os, and $^{40}\text{Ar}/^{39}\text{Ar}$ geochronology of porphyry Sn ± Cu ± Mo and polymetallic (Ag–Pb–Zn–Cu) vein mineralization at Bianjiadayuan, Inner Mongolia, northeast China; implications for discrete mineralization events. *Economic Geology* **112**, 2041–59.
- Zhai DG, Liu JJ, Zhang HY, Tombros S and Zhang AL** (2018b) A magmatic–hydrothermal origin for Ag–Pb–Zn vein formation at the Bianjiadayuan deposit, inner Mongolia, NE China: evidence from fluid inclusion, stable (C–H–O) and noble gas isotope studies. *Ore Geology Reviews* **101**, 1–16.
- Zhang HY, Zhai DG, Liu JJ, Li PL, Li K and Sun HJ** (2019) Fluid inclusion and stable (H–O–C) isotope studies of the giant Shuangjianzishan epithermal Ag–Pb–Zn deposit, Inner Mongolia, NE China. *Ore Geology Reviews* **115**, 103170.
- Zhang LG** (1985) *Geological Appliance for the Stable Isotope*. Shanxi: Shanxi Science and Technology Publishing House, pp. 54–61 (in Chinese).
- Zhang LG** (1989) *Diagenetic–Metallogenic Theory and Exploration*. Beijing: Beijing University of Technology Publishing House, pp. 84–139 (in Chinese).
- Zhang XB** (2017) Pb–Zn polymetallic deposits metallogenic series and prospecting direction of the west slope of southern Great Xing'an Range. Ph.D. thesis. Changchun: Jilin University. Published thesis (in Chinese with English abstract).
- Zhang XJ, Zhang LC, Jin XD, Wu HY, Xiang P and Chen ZG** (2010) U–Pb ages, geochemical characteristics and their implications of Banlashan molybdenum deposit. *Acta Petrologica Sinica* **26**, 1411–22.
- Zhang XX, Su Z and Gao YF** (2017) Zircon U–Pb geochronology and geochemistry of the Early Cretaceous volcanic rocks from the Manitu Formation in the Hongol Area, northeastern Inner Mongolia. *Acta Geologica Sinica* **91**, 1286–304.
- Zhou ZH, Mao JW and Lyckberg P** (2012) Geochronology and isotopic geochemistry of the A-type granites from the Huanggang Sn–Fe deposit, southern Great Hinggan Range, NE China: Implication for their origin and tectonic setting. *Journal of Asian Earth Sciences* **49**, 272–86.